

CARBON NANOMATERIALS SOURCEBOOK

VOLUME I



Graphene, Fullerenes, Nanotubes,
and Nanodiamonds

Edited by

Klaus D. Sattler



CRC Press
Taylor & Francis Group

CARBON NANOMATERIALS SOURCEBOOK

Graphene, Fullerenes, Nanotubes,
and Nanodiamonds

This page intentionally left blank

CARBON NANOMATERIALS SOURCEBOOK

VOLUME I

Graphene, Fullerenes, Nanotubes,
and Nanodiamonds

Edited by

Klaus D. Sattler

University of Hawaii at Manoa, Honolulu, USA

 **CRC Press**
Taylor & Francis Group
Boca Raton London New York

CRC Press is an imprint of the
Taylor & Francis Group, an **informa** business

CRC Press
Taylor & Francis Group
6000 Broken Sound Parkway NW, Suite 300
Boca Raton, FL 33487-2742

© 2016 by Taylor & Francis Group, LLC
CRC Press is an imprint of Taylor & Francis Group, an Informa business

No claim to original U.S. Government works
Version Date: 20160301

International Standard Book Number-13: 978-1-4822-5269-9 (eBook - PDF)

This book contains information obtained from authentic and highly regarded sources. Reasonable efforts have been made to publish reliable data and information, but the author and publisher cannot assume responsibility for the validity of all materials or the consequences of their use. The authors and publishers have attempted to trace the copyright holders of all material reproduced in this publication and apologize to copyright holders if permission to publish in this form has not been obtained. If any copyright material has not been acknowledged please write and let us know so we may rectify in any future reprint.

Except as permitted under U.S. Copyright Law, no part of this book may be reprinted, reproduced, transmitted, or utilized in any form by any electronic, mechanical, or other means, now known or hereafter invented, including photocopying, microfilming, and recording, or in any information storage or retrieval system, without written permission from the publishers.

For permission to photocopy or use material electronically from this work, please access www.copyright.com (<http://www.copyright.com/>) or contact the Copyright Clearance Center, Inc. (CCC), 222 Rosewood Drive, Danvers, MA 01923, 978-750-8400. CCC is a not-for-profit organization that provides licenses and registration for a variety of users. For organizations that have been granted a photocopy license by the CCC, a separate system of payment has been arranged.

Trademark Notice: Product or corporate names may be trademarks or registered trademarks, and are used only for identification and explanation without intent to infringe.

Visit the Taylor & Francis Web site at
<http://www.taylorandfrancis.com>

and the CRC Press Web site at
<http://www.crcpress.com>

Contents

Preface.....	vii
Editor	ix
Contributors	xi

SECTION I Graphene

1 Suspended Graphene	3
<i>Hong Koo Kim and Myungji Kim</i>	
2 Graphene Quantum Dots.....	29
<i>Christian Volk, Christoph Neumann, Stephan Engels, Alexander Epping, and Christoph Stampfer</i>	
3 Graphene Network	67
<i>Mashkoor Ahmad, Irum Khalid, Ayousha Ayaz, and Muhammad Hussain</i>	
4 Covalently Functionalized Graphene	89
<i>Pablo A. Denis</i>	
5 Few-Layer Graphene Oxide in Tribology	107
<i>Adolfo Senatore and Maria Sarno</i>	
6 Graphene Oxide Nanodisks and Nanodots	131
<i>Sambandam Anandan and Muthupandian Ashokkumar</i>	
7 Natural Graphene-Based Shungite Nanocarbon	153
<i>Natalia N. Rozhkova, Sergey P. Rozhkov, and Andrey S. Goryunov</i>	

SECTION II Fullerenes

8 Solid Fullerenes under Compression	179
<i>Jianfu Li, Bolong Huang, and Rui-Qin Zhang</i>	
9 Open-Cage Fullerenes	193
<i>Argyro T. Papastavrou, Eleftherios K. Pefkianakis, Manolis M. Roubelakis, and Georgios C. Vougioukalakis</i>	

10	Endohedral Fullerenes: Optical Properties and Biomedical Applications... 259 <i>Panagiotis Dallas, Ilija Rašović, Gregory Rogers, and Kyriakos Porfyrakis</i>	259
11	Carbon Nano-Onions..... 275 <i>Diana M. Brus, Olena Mykhailiv, Luis Echegoyen, and Marta E. Plonska-Brzezinska</i>	275
12	Endohedral Clusterfullerenes 303 <i>Alexey Popov</i>	303

SECTION III Nanotubes

13	CVD-Synthesized Carbon Nanotubes337 <i>Maria Sarno and Adolfo Senatore</i>	337
14	Carbon Nanotube Fibers357 <i>Jandro L. Abot and Cijo Punnakattu Rajan</i>	357
15	Endohedrally Doped Carbon Nanotubes 385 <i>Hidetsugu Shiozawa</i>	385
16	Functionalized Carbon Nanotubes.....415 <i>Vivian Machado de Menezes</i>	415
17	Carbon Nanotube Networks 429 <i>Luca Camilli</i>	429
18	Carbon Nanotubes for Sensing Applications 443 <i>Abha Misra</i>	443
19	Biomedical Carbon Nanotubes 455 <i>Diogo Mata, Maria H. Fernandes, Maria A. Lopes, and Rui F. Silva</i>	455
20	Ultrashort Carbon Nanocapsules for Biomedicine491 <i>Stuart J. Corr, Steven A. Curley, and Lon J. Wilson</i>	491

SECTION IV Nanodiamonds

21	Detonation Nanodiamonds..... 509 <i>Valerie Dolmatov</i>	509
22	Surface-Modified Nanodiamonds525 <i>Wesley Wei-Wen Hsiao, Hsin-Hung Lin, Feng-Jen Hsieh, and Huan-Cheng Chang</i>	525
23	Cargo-Delivering Nanodiamonds 543 <i>Basem Moosa and Niveen M. Khashab</i>	543
24	Nanodiamonds in Biomedicine557 <i>Saniya Alwani and Ildiko Badea</i>	557
Index		591

Preface

In the last three decades, zero-dimensional, one-dimensional, and two-dimensional carbon nanomaterials have attracted significant attention because of their unique electronic, optical, thermal, mechanical, and chemical properties. There is a need for understanding the science of carbon nanomaterials, the production methods, and the applications, to use these exceptional properties. In particular, in the last two decades, carbon nanotubes, fullerenes, nanodiamonds, and mesoporous carbon nanostructures became a new class of nanomaterials. Research on graphene, a single sheet of graphite, is one of the fastest growing fields today and holds the promise of someday replacing silicon in computers and electronic devices. Many scientists and engineers are redirecting their work toward carbon nanomaterials. It is in this context that the editor of this work determined that a new resource concentrating on this subject would be a unique and useful source of information and learning.

Carbon Nanomaterials Sourcebook is the most comprehensive reference that covers the field of carbon nanomaterials, reflecting its interdisciplinary nature that brings together physics, chemistry, materials science, molecular biology, engineering, and medicine. The two volumes describe fundamental properties, growth mechanisms, and processing of nanocarbons as well as their functionalization for electronic device, energy conversion and storage, and biomedical and environmental applications. It encompasses a wide range of areas from science to engineering. Moreover, in addition to addressing the latest advances, the *Sourcebook* presents core knowledge with basic mathematical equations, tables, and graphs to provide the reader with the tools necessary to understand current and future technology developments.

The contents are made up of 54 total chapters organized into nine subject areas, with each chapter covering one type of carbon nanomaterial. Materials have been selected to showcase exceptional properties, good synthesis and large-scale production methods, and strong current and future application prospects. Every chapter covers the three main areas: formation, properties, and applications. This setup makes the book a unique source where a reader can easily navigate to find the information about a particular material. The chapters will be written in tutorial style, where basic equations and fundamentals are included in an extended introduction.

This page intentionally left blank

Editor

Klaus D. Sattler pursued his undergraduate and master's courses at the University of Karlsruhe in Germany. He received his PhD under the guidance of Professors G. Busch and H.C. Siegmann at the Swiss Federal Institute of Technology (ETH) in Zurich, where he was among the first to study spin-polarized photoelectron emission. In 1976, he began a group for atomic cluster research at the University of Konstanz in Germany, where he built the first source for atomic clusters and led his team to pioneering discoveries such as “magic numbers” and “Coulomb explosion.” He was at the University of California, Berkeley, for three years as a Heisenberg fellow, where he initiated the first studies of atomic clusters on surfaces with a scanning tunneling microscope.

Dr. Sattler accepted a position as professor of physics at the University of Hawaii, Honolulu, in 1988. There, he initiated a research group for nanophysics, which, using scanning probe microscopy, obtained the first atomic-scale images of carbon nanotubes directly confirming the graphene network. In 1994, his group produced the first carbon nanocones. He has also studied the formation of polycyclic aromatic hydrocarbons and nanoparticles in hydrocarbon flames in collaboration with ETH Zurich. Other research has involved the nanopatterning of nanoparticle films, charge density waves on rotated graphene sheets, bandgap studies of quantum dots, and graphene folds. His current work focuses on novel nanomaterials and solar photocatalysis with nanoparticles for the purification of water.

He is the editor of the seven-volume *Handbook of Nanophysics* (CRC Press, 2011) and *Fundamentals of Picoscience* (CRC Press, 2014). Among his many other accomplishments, Dr. Sattler was awarded the prestigious Walter Schottky Prize from the German Physical Society in 1983. At the University of Hawaii, he teaches courses in general physics, solid state physics, and quantum mechanics.

This page intentionally left blank

Contributors

Jandro L. Abot

Department of Mechanical Engineering
The Catholic University of America
Washington, District of Columbia

Mashkoor Ahmad

Nanomaterials Research Group (NRG)
Physics Division
PINSTECH
Nilore, Islamabad, Pakistan

Saniya Alwani

Drug Discovery and Development Research
Group
College of Pharmacy and Nutrition
University of Saskatchewan
Saskatoon, Saskatchewan, Canada

Sambandam Anandan

Nanomaterials & Solar Energy Conversion Lab
Department of Chemistry
National Institute of Technology
Trichy, India

Muthupandian Ashokkumar

School of Chemistry
University of Melbourne
Victoria, Australia

Ayousha Ayaz

Nanomaterials Research Group (NRG)
Physics Division
PINSTECH
Nilore, Islamabad, Pakistan

Ildiko Badea

Drug Discovery and Development Research
Group
College of Pharmacy and Nutrition
University of Saskatchewan
Saskatoon, Saskatchewan, Canada

Diana M. Brus

Institute of Chemistry
University of Bialystok
Bialystok, Poland

Luca Camilli

Department of Micro and Nanotechnology
Technical University of Denmark
Kongens Lyngby, Denmark

Huan-Cheng Chang

Institute of Atomic and Molecular Sciences
Academia Sinica
Taipei, Taiwan

Stuart J. Corr

Department of Surgery
Baylor College of Medicine
and
Department of Chemistry
and
Richard E. Smalley Institute for Nanoscale
Science & Technology
Rice University
Houston, Texas

Steven A. Curley

Department of Surgery
 Baylor College of Medicine
 and
 Department of Mechanical Engineering
 and Materials Science
 Rice University
 Houston, Texas

Panagiotis Dallas

Department of Materials
 University of Oxford
 Oxford, United Kingdom

Pablo A. Denis

Computational Nanotechnology
 DETEMA
 Facultad de Química
 UDELAR
 Montevideo, Uruguay

Valerie Dolmatov

Federal State Unitary Enterprise
 Special Design and Technology Bureau
 Russia

Luis Echegoyen

Department of Chemistry
 University of Texas at El Paso
 El Paso, Texas

Stephan Engels

JARA-FIT and II
 Institute of Physics
 RWTH Aachen University
 Aachen, Germany

and

Peter Grünberg Institute (PGI-9)
 Forschungszentrum Jülich
 Jülich, Germany

Alexander Epping

JARA-FIT and II
 Institute of Physics
 RWTH Aachen University
 Aachen, Germany

and

Peter Grünberg Institute (PGI-9)
 Forschungszentrum Jülich
 Jülich, Germany

Maria H. Fernandes

Laboratory for Bone Metabolism and
 Regeneration
 Faculty of Dental Medicine
 University of Porto
 Porto, Portugal

Andrey S. Goryunov

Institute of Biology Karelian Research Center
 RAS
 Petrozavodsk, Russia

Wesley Wei-Wen Hsiao

Institute of Atomic and Molecular Sciences
 Academia Sinica
 Taipei, Taiwan

Feng-Jen Hsieh

Institute of Atomic and Molecular Sciences
 Academia Sinica
 Taipei, Taiwan

Bolong Huang

Department of Physics and Materials Science
 City University of Hong Kong

Muhammad Hussain

Nanomaterials Research Group (NRG)
 Physics Division
 PINSTECH
 Nilore, Islamabad, Pakistan

Irum Khalid

Nanomaterials Research Group (NRG)
 Physics Division
 PINSTECH
 Nilore, Islamabad, Pakistan

Niveen M. Khashab

Smart Hybrid Materials (SHMs)
Advanced Membranes and Porous Materials
Center
King Abdullah University of Science
and Technology
Thuwal, Kingdom of Saudi Arabia

Hong Koo Kim

Department of Electrical and Computer
Engineering
and
Petersen Institute of NanoScience
and Engineering
University of Pittsburgh
Pittsburgh, Pennsylvania

Myungji Kim

Department of Electrical and Computer
Engineering
and
Petersen Institute of NanoScience
and Engineering
University of Pittsburgh
Pittsburgh, Pennsylvania

Jianfu Li

Department of Physics and Materials Science
City University of Hong Kong
Kowloon Tong, Hong Kong

Hsin-Hung Lin

Institute of Atomic and Molecular Sciences
Academia Sinica
Taipei, Taiwan

and

Institute of Engineering in Medicine
University of California, San Diego
La Jolla, California

Maria A. Lopes

CEMUC
Metallurgical and Materials Engineering
Department
Faculty of Engineering
University of Porto
Porto, Portugal

Vivian Machado de Menezes

Universidade Federal da Fronteira Sul–UFFS
Laranjeiras do Sul, PR, Brazil

Diogo Mata

CICECO
Materials and Ceramic Engineering
Department
University of Aveiro
Aveiro, Portugal

Abha Misra

Department of Instrumentation and Applied
Physics
Indian Institute of Science
Bangalore, Karnataka, India

Basem Moosa

Smart Hybrid Materials (SHMs)
Advanced Membranes and Porous Materials
Center
King Abdullah University of Science
and Technology
Thuwal, Kingdom of Saudi Arabia

Olena Mykhailiv

Institute of Chemistry
University of Bialystok
Bialystok, Poland

Christoph Neumann

JARA-FIT and II
Institute of Physics
RWTH Aachen University
Aachen, Germany

and

Peter Grünberg Institute (PGI-9)
Forschungszentrum Jülich
Jülich, Germany

Argyro T. Papastavrou

Laboratory of Organic Chemistry
Department of Chemistry
University of Athens
Panepistimiopolis, Athens, Greece

Eleftherios K. Pefkianakis

Laboratory of Organic Chemistry
Department of Chemistry
University of Athens
Panepistimiopolis, Athens, Greece

Marta E. Plonska-Brzezinska

Institute of Chemistry
University of Bialystok
Bialystok, Poland

Alexey Popov

Leibniz Institute for Solid State and Materials
Research (IFW Dresden)
Dresden, Germany

Kyriakos Porfyrakis

Department of Materials
University of Oxford
Oxford, United Kingdom

Cijo Punnakattu Rajan

Department of Mechanical Engineering
The Catholic University of America
Washington, District of Columbia

Ilija Rašović

Department of Materials
University of Oxford
Oxford, United Kingdom

Gregory Rogers

Department of Materials
University of Oxford
Oxford, United Kingdom

Manolis M. Roubelakis

Laboratory of Organic Chemistry
Department of Chemistry
University of Athens
Panepistimiopolis, Athens, Greece

Sergey P. Rozhkov

Institute of Biology Karelian Research Center
RAS
Petrozavodsk, Russia

Natalia N. Rozhkova

Institute of Geology Karelian Research Center
RAS
Petrozavodsk, Russia

Maria Sarno

Department of Industrial Engineering
and
NANO_MATES Research Centre
University of Salerno
Salerno, Italy

Adolfo Senatore

Department of Industrial Engineering
and
NANO_MATES Research Centre
University of Salerno
Salerno, Italy

Hidetsugu Shiozawa

Faculty of Physics
University of Vienna
Vienna, Austria

Rui F. Silva

CICECO
Materials and Ceramic Engineering Department
University of Aveiro
Aveiro, Portugal

Christoph Stampfer

JARA-FIT and II
Institute of Physics
RWTH Aachen University
Aachen, Germany

and

Peter Grünberg Institute (PGI-9)
Forschungszentrum Jülich
Jülich, Germany

Christian Volk

JARA-FIT and II
Institute of Physics
RWTH Aachen University
Aachen, Germany

and

Peter Grünberg Institute (PGI-9)
Forschungszentrum Jülich
Jülich, Germany

Georgios C. Vougioukalakis

Laboratory of Organic Chemistry
Department of Chemistry
University of Athens
Panepistimiopolis, Greece

Lon J. Wilson

Department of Chemistry
and
Richard E. Smalley Institute for Nanoscale
Science & Technology
Rice University
Houston, Texas

Rui-Qin Zhang

Department of Physics and Materials Science
City University of Hong Kong
Hong Kong SAR, China

This page intentionally left blank

I

Graphene

This page intentionally left blank

1

Suspended Graphene

1.1	Introduction	3
1.2	Fabrication	5
1.3	Low-Voltage Emission of 2D Electron Gas.....	8
	Calculation of 2DEG Density in a MOS Capacitor Structure • Space-Charge-Limited Current Flow of 2DEG in a Nanoscale Void Channel	
1.4	Electron Capture and Transmission at Dark Forward Bias.....	13
	Emission and Transport of 2DEG • Space Charge Neutralization by Suspended Graphene • Calculation of 2DEG Density in Graphene/SiO ₂ /Si	
1.5	Electron Capture and Transmission at Photo Reverse Bias.....	19
	Photo-Induced 2DEG Inversion Layer • Emission and Transport of Photocarrier 2DEG	
1.6	Conclusion	23
	Acknowledgments.....	23
	References.....	24

Hong Koo Kim

Myungji Kim

1.1 Introduction

Graphene, a one-atom-thick carbon crystal in a honeycomb lattice, possesses many fascinating properties originating from the manifold potential for interactions at electronic, atomic, or molecular levels (Novoselov et al. 2004, 2005; Zhang et al. 2005; Geim & Novoselov 2007; Schedin et al. 2007; Bolotin et al. 2009; Geim 2009; Neto et al. 2009; Kotov et al. 2012). Graphene is remarkably strong for its atomic thinness and conducts heat and electricity with great efficiency. Electron motion in graphene is essentially governed by Dirac's relativistic equation. The charge carriers in graphene behave like relativistic particles with zero rest mass and have an effective "speed of light" of $\sim 10^6$ m s⁻¹. For a perfect graphene sheet free from impurities and disorder, the Fermi level lies at the so-called Dirac point, where the density of electronic states vanishes. Unlike the two-dimensional (2D) electron system in conventional semiconductors, where the charge carriers become immobile at low densities, the carrier mobility in graphene can remain very high, even with vanishing density of states at Dirac point (Du et al. 2008; Morozov et al. 2008).

Every carbon atom of graphene is on the surface and is therefore easily accessible from both sides. This surface-only nature renders graphene prone to interactions with (and disturbances from) surrounding atoms and molecules. Many of the predicted properties arising from the 2D nature of graphene can be significantly altered by perturbations from an underlying substrate or adsorbates (Hwang et al. 2007; Adam & Sarma 2008; Chen et al. 2008). Substrates, for example, introduce scattering centers, dopants, and corrugations that can obscure graphene's intrinsic properties. Suspended graphene structures have drawn increasing attention, driven by the motivations of exploring intrinsic/ultimate properties of graphene and also of exploring new applications that would not be possible with substrate-bound graphene,

such as nanoelectromechanical resonators or transelectrode membranes (Bunch et al. 2008; Garaj et al. 2010; Hu et al. 2014).

From the perspective of thermodynamic stability, perfect crystals cannot exist in 2D space (Mermin 1968; Landau & Lifshitz 1980). Near-perfect crystals, however, can exist in 3D space through bending in the third dimension. A transmission electron microscopy study revealed that suspended graphene sheets are not perfectly flat but exhibit nanometer-scale random elastic deformations (out-of-plane deformation of ~ 1 nm and the surface normal varying by several degrees) (Figure 1.1) (Meyer et al. 2007). The interaction between bending and stretching long-wavelength phonons is believed to stabilize atomically thin membranes through their nanometer-scale deformation in the third dimension.

By isolating graphene from external sources of scattering, electron mobility exceeding $200,000 \text{ cm}^2/\text{Vs}$ was demonstrated, which corresponds to a more than 10-fold enhancement compared with the conventional graphene on substrate (Figure 1.1) (Bolotin et al. 2008). It is interesting to note that this dramatic enhancement of carrier mobility required an annealing (current-induced Joule heating) of suspended

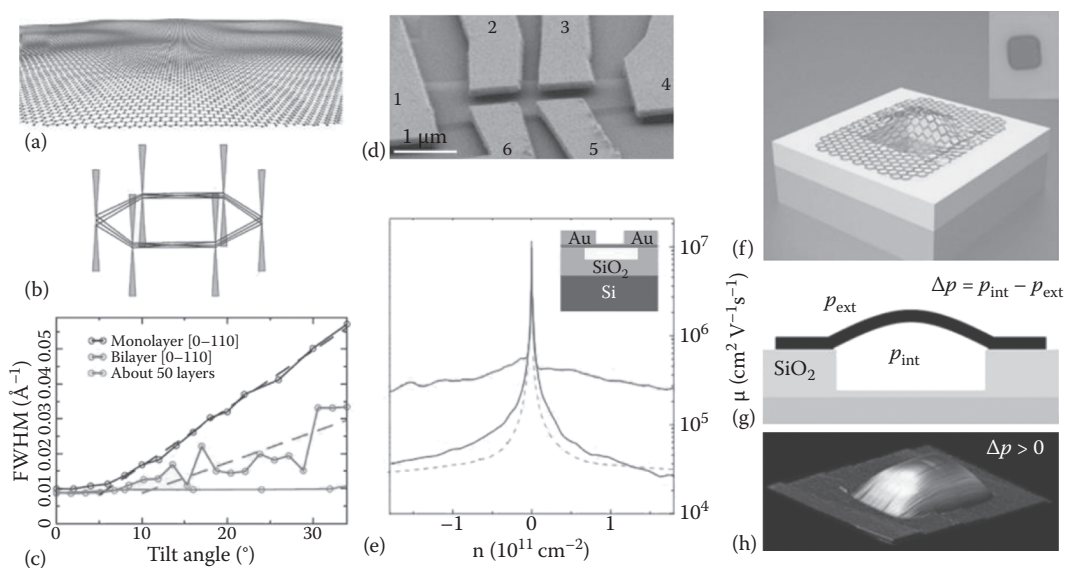


FIGURE 1.1 Morphology of suspended graphene (a–c). (a) A perspective view illustrating microscopic corrugation. The roughness shown imitates quantitatively the roughness found experimentally. (b) A superposition of the diffracting beams from microscopic flat areas effectively turns the rods (reciprocal space) into cone-shaped volumes so that diffraction spots become blurred at large angles. (c) Full-width half-maximum (FWHM) for the (0110) diffraction peak in monolayer and bilayer membranes and thin graphite (as a reference), as a function of tilt angle. Graphene roughness is measured from the diffraction patterns obtained at different tilt angles. In-plane carrier transport of suspended graphene (d, e). (d) SEM image of a suspended six-probe graphene device. (e) Mobility measured as a function of carrier density: before (middle, solid) and after (top, solid) current annealing; data from a traditional high-mobility device on substrate (bottom, dotted line) are shown for comparison. (Inset) device schematic, side view. Impermeable atomic membrane from graphene sheets (f–h). (f) Schematic of a graphene sealed microchamber. (Inset) optical image of a single atomic layer graphene drumhead on 440-nm-thick SiO₂. The dimensions of the microchamber are $4.75 \mu\text{m} \times 4.75 \mu\text{m} \times 380 \text{ nm}$. (g) Side view schematic. (h) AFM image of a ~ 9 -nm-thick many-layer graphene drumhead with $\Delta p > 0$. The upward deflection at the center of the membrane is 90 nm. Reprinted by permission from MacMillan Publishers Ltd. *Solid State Commun.* Meyer, J.C., Geim, A.K., Katsnelson, M.I., *Nature*, 446, 60–63, 2007. Copyright 2007. d, e, Reprinted from *Solid State Commun.*, 146, Bolotin, K.I., Sikes, K.J., Jiang, Z. et al., Ultrahigh electron mobility in suspended graphene, 351–355. Copyright 2008, with permission from Elsevier. f–h, Reprinted with permission from Bunch, J.S., Verbridge, S.S., Alden, J.S. et al., *Nanosci. Lett.*, 8, 2458–2462, 2008. Copyright 2008 American Chemical Society.)

graphene, which is designed to desorb adsorbates on either side of graphene. This suggests that impurities trapped between the substrate (SiO_2) and graphene are limiting the mobility of unsuspended graphene.

Graphene is shown to have high adhesion energy ($\sim 0.45 \text{ J m}^{-2}$), which is much larger than those measured in conventional micromechanical structures and is comparable with solid–liquid adhesion energies (Koenig et al. 2011). By pressing on suspended graphene with an atomic force microscope (AFM) tip with calibrated spring constant, atomic layers of graphene are shown to have large stiffness values, similar to bulk graphite ($E \sim 1 \text{ TPa}$) (Frank et al. 2007; Lee et al. 2008). The impermeability of suspended graphene to gas molecules is also demonstrated (Figure 1.1) (Bunch et al. 2008). By applying a pressure difference across the membrane, both the elastic constants and the mass of a monolayer graphene were measured. The atomically thin sealed chambers can support pressures up to a few atmospheres. By adjusting the pressure difference, thereby the strain of suspended graphene, the mechanical resonance frequency was tuned by $\sim 100 \text{ MHz}$.

Graphene is known to have an anomalously large, negative thermal expansion coefficient (Bao et al. 2009). This can cause a large amount of thermal stress/strain depending on the substrate material and the amount of temperature change. A flat suspended graphene, exfoliation-transferred to a trench on SiO_2/Si substrate, exhibits ripples (up to $\sim 30 \text{ nm}$ amplitude) after experiencing a thermal treatment (heating or cooling) by $100\text{--}200 \text{ K}$ (Bao et al. 2009).

Graphene is transmissive to impinging electrons while being impermeable to atoms and molecules (Bunch et al. 2008). Harboring a 2D electron system (2DES) (Ando et al. 1982; Eisenstein et al. 1992; Ho et al. 2009; Li et al. 2011), graphene is expected to be interactive with out-of-plane incident electrons as well. A graphene electrode suspended on a nanoscale void channel (trenches or holes) provides an interesting configuration to investigate the interplay of in- and out-of-plane interactions of 2DESs mediated by electron transport in vacuum.

At electron energy $< \sim 10 \text{ eV}$, the de Broglie wavelength becomes greater than the lattice atomic spacing and crystalline diffraction is less likely to occur. Below $5\text{--}10 \text{ eV}$, the dominant scattering mechanism is expected to involve inelastic interactions such as electron excitations or electron–phonon interactions (Kuhr & Fitting 1999; Müllerová et al. 2010; Cazaux 2012). The damage threshold of graphene is known to be $>15 \text{ eV}$, corresponding to incident electron energy $>80 \text{ keV}$ (Crespi et al. 1996; Krasheninnikov & Nordlund 2010; Börrnert et al. 2012). Considering the relatively large threshold, electrons of very low energy ($<5 \text{ eV}$) are expected to induce no damage to graphene (Srisonphan et al. 2014).

In this chapter, we review the emission, capture, and transmission interactions with very-low-energy electrons and explore the potential of using graphene as an electron-transparent grid in low-voltage nanoscale vacuum electronic devices (Child 1911; Langmuir 1913; Spindt et al. 1976; Han et al. 2012; Srisonphan et al. 2012; Stoner & Glass 2012). The electron transparency of graphene has been the subject of debate in recent literature (Müllerová et al. 2010; Li et al. 2014). Most studies were performed in transmission electron microscopes at relatively high energies ($\gg 100 \text{ eV}$) or in electron holography mode at low energies ($\sim 100 \text{ eV}$) demonstrating transparencies $>70\%$ (Kreuzer et al. 1992; Morin et al. 1996; Mutus et al. 2011). In the case of very-low-energy electrons ($<5 \text{ eV}$), however, reports are rare. Most work was performed in a triode (three-terminal) configuration, where the anode potential is designed to be sufficiently high to collect incoming electrons transmitted through a graphene grid; therefore, the field distribution around the graphene is inevitably altered by the anode field. In this study, we employ a diode (two-terminal) configuration and investigate the direct interplay of cathode and anode/grid (graphene) mediated by the ballistic transport of electrons through a nanoscale gap in air ambient (Srisonphan et al. 2014).

1.2 Fabrication

Suspended graphene can be fabricated with or without involving a transfer process. In the case of a non-transfer method, a graphene layer is initially grown on a chosen substrate, usually on a Cu or Ni foil by chemical vapor deposition (CVD) or on a SiC substrate by Si sublimation or by CVD (Jernigan et al. 2009;

Shivaraman et al. 2009; Mattevi et al. 2011; Suk et al. 2011). In the case of graphene on a metal substrate, the bottom side is lithographically patterned and etched away in a chemical solution. In the case of graphene on SiC, an undercut etching is performed through a lithographically defined etch mask. This substrate removal process leaves a graphene membrane supported by an unetched part of substrate.

In the case of a transfer method, a graphene flake is placed on a predefined microstructure (trench, hole, or grid) formed in a substrate (Meyer et al. 2007). Precision placement of graphene on a predetermined microstructure would be challenging, if it is a small size flake. In an alternative transfer method, a graphene flake is placed on a substrate and then metal electrodes are lithographically defined on top (Bolotin et al. 2008). An undercut etching is then performed to remove the substrate material underneath the graphene. Compared with the nontransfer method discussed previously, the transfer method generally allows a greater degree of freedom/flexibility in integrating with other functional substrates/devices.

In this study, we have employed the transfer method with CVD-grown graphene onto nanoscale trenches/holes formed in a SiO₂/Si substrate (Figure 1.2). CVD growth of graphene on metallic substrates is a well-established technique yielding large graphene flakes to a commercially viable scale (Kim et al. 2009; Li et al. 2009). Although CVD-grown graphene generally shows lower electron mobility and more defects than does graphene produced by an exfoliation method, the easy transfer from the metal substrate to other substrates is expected to enable many device applications at chip or wafer level.

First, a SiO₂ layer (~20 nm thickness) was grown by thermal oxidation on p-type Si (B-doped, 10 Ω-cm resistivity) or n-type Si (P-doped, 5 Ω-cm resistivity) wafers [(100)-oriented; 525 μm thickness]. A bottom-side electrode was prepared by depositing a 150-nm-thick Al layer (5 N purity) on Si by thermal evaporation, followed by Ohmic contact annealing at 350°C. Vertically etched trench or hole structures were then formed by employing a nanoscale patterning/lithography technique, such as focused ion beam (FIB) etching or electron-beam lithography (EBL), or photolithography in conjunction with use of plasma reactive ion etching (RIE).

FIB etching directly etches nanoscale patterns into substrate without involving an etch mask or a subsequent pattern transfer process. In this study, FIB etching was performed with the Seiko Dual Beam System (SMI-3050SE). A Ga ion beam (30 keV; 94 pA) was used with 0.5-μs dwell time in creating square wells, holes, or trenches with minimum lateral dimensions (trench width or hole diameter) down to ~70 nm and an etch depth up to 1–2 μm.

In the case of photolithography, a 50-nm-thick Cr layer was deposited on SiO₂/Si substrate by thermal evaporation (Figure 1.2a). A window of narrow stripe patterns (5–50 μm width; single or multiple channels of 8–10 mm length) was then opened in the Cr layer by performing photolithography and RIE. The Cr window etching was performed in Cl₂/O₂ ambient with an inductively coupled plasma RIE (ICP-RIE) system (Unaxis 790 ICP-RIE). Subsequently, a trench etching was performed to 500–1000 nm depth by RIE in CF₄/O₂ ambient with use of the Cr window as an etch mask. The remaining photoresist was removed in acetone. The Cr mask was removed in Cr etchant [NaOH:K₃Fe(CN)₆:H₂O = 2 g:6 g:22 mL].

In the case of EBL, an e-beam resist, polymethylmethacrylate (PMMA, ~200 nm thickness) was spin-coated on the SiO₂/Si substrate (Figure 1.2b). EBL was then performed using the Raith e-Line system (10 keV, beam current, 220 pA) to define trench/hole patterns (with minimum lateral dimension of ~70 nm). The exposed PMMA was developed, and the EBL-defined pattern was subsequently transferred to SiO₂/Si substrate (to 100–200 nm etch depth) by performing RIE in CF₄/O₂ ambient with the PMMA pattern as an etch mask. A residual PMMA was removed in acetone.

Finally, a monolayer graphene was transferred to the trench/hole-etched SiO₂/Si substrate (Figure 1.2c) (Suk et al. 2011). To place a graphene membrane suspended on the etched SiO₂/Si substrate, we started with a monolayer graphene grown on Cu foil (purchased from ACS Material; CVD grown on 25-μm-thick Cu foil). A PMMA layer (MicroChem 950 PMMA A7, 4% in anisole) was spun-coated on the graphene-covered Cu foil (0.3 × 0.4 cm²). The Cu foil was etched away in ferric chloride solution (Transene Cu Etchant CE-100). After ~30 min etching, the PMMA/graphene stacked film was floating in the etchant solution. A clear glass substrate was then submerged into the solution to lift the floating film. The film was then transferred to deionized (DI) water and was left floating for 10 min. This process

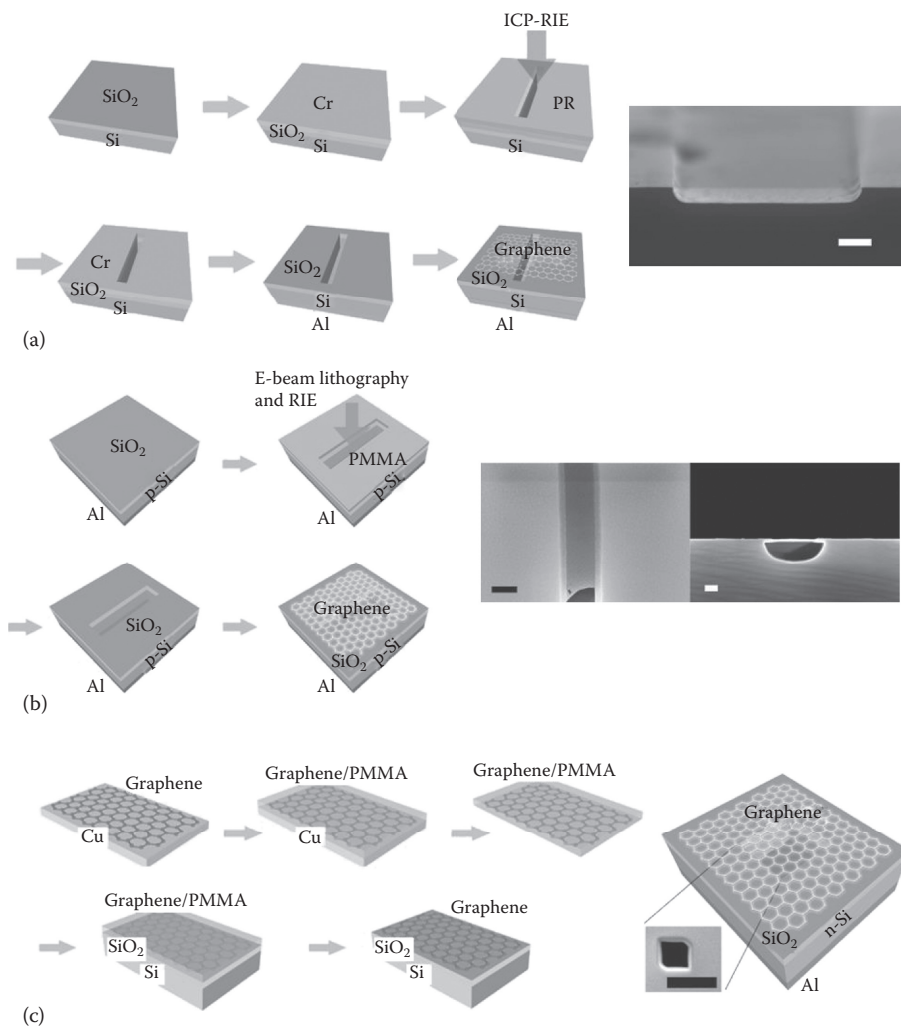


FIGURE 1.2 Fabrication of graphene suspended on a channel-etched SiO₂/Si substrate. (a) Process flow employing photolithography and RIE for channel etching. (Right) SEM image of suspended graphene on a trench-etched substrate. Scale bar, 1 μm. (b) Process flow employing EBL and RIE for channel etching. (Right) SEM images of suspended graphene: top view, left (scale bar, 300 nm); cross-section, right (scale bar, 100 nm). (c) Transfer process of CVD grown graphene onto a channel-etched substrate. (Right) SEM image of suspended graphene on a FIB-etched substrate. Scale bar, 1 μm.

(transfer to DI water) was repeated at least 3 times to remove residual etchant. A target substrate (trench/hole-etched SiO₂/Si wafer) was then immersed into the DI water, and the PMMA/graphene film was lifted up while being positioned by a needle. The PMMA/graphene stack, placed on the target substrate, was dried at ~70°C in air for 2 h to enhance adhesion of graphene to the substrate. The PMMA was removed in acetone, followed by rinse in methanol and DI water. Finally, the sample was dried at ~70°C for 2 h to remove moisture trapped in the void-channel. It should be mentioned that graphene is known to remain stable in humid oxygen ambient at up to 400°C (Liu et al. 2008). Therefore, thermal oxidation is not an issue to worry about during baking. Rather, a large thermal expansion mismatch with substrate is more the issue that may cause wrinkles in suspended graphene (Bao et al. 2009). Therefore, the post-transfer baking temperature needs to be in the moderate or mild range.

1.3 Low-Voltage Emission of 2D Electron Gas

In generating a constant flux of very-low-energy electrons, we exploit the phenomenon that a 2D electron gas (2DEG) induced at the SiO₂/Si interface of a metal-oxide-semiconductor (MOS) structure can easily emit into air (void channel) at low voltage (~ 1 V) (Srisophon et al. 2012). This low-voltage emission, enabled by Coulombic repulsion of electrons in 2DEG, has the effect of negative electron affinity and demonstrates high current density emission ($\sim 10^5$ A/cm²). The emitted electrons ballistically travel in the nanovoid channel. The channel length (i.e., the thickness of oxide layer) is designed to be smaller than the mean free path of electrons in air (~ 60 nm). Therefore, emitted electrons should travel scattering-free in the ambient (air) channel, as if in a vacuum. The transit time is estimated to be 10–100 fs for 10–20-nm-thick SiO₂ at 1–10 V bias.

A MOS capacitor structure can harbor a quasi-2DES in a potential well (~ 2 nm width) developed in the semiconductor side (Ando et al. 1982; Toriumi et al. 1986). The metal side also develops band bending, accommodating charges of opposite polarity in a confined space (< 1 nm) at the interface with the oxide layer (Mead 1961; Black & Welser 1999). Electrons residing inside the bulk Si of a MOS structure are basically confined by energy barriers at the surface (with air) and at the interface (with SiO₂), typically with a vacuum barrier greater than the SiO₂ barrier. Therefore, electrons cannot easily emit into air, unless the energy barrier is significantly lowered for thermionic or field emission. (Also, we note that in this work, the oxide layer thickness is designed to be ~ 20 nm; therefore, direct tunneling through the oxide barrier layer remains completely negligible.)

The situation can be very different for the electrons confined in a 2DEG layer. First, let us imagine an infinite extension of 2DEG formed at SiO₂/Si (Figure 1.3). The overall charge neutrality condition is maintained between the 2DEG (and also depletion charge) in Si and the positive charges induced in the metal side. Along the in-plane direction of 2DEG, Coulombic repulsion among electrons will cancel out because of the symmetry of electron distribution. Now, consider a MOS structure whose lateral extent is finite; i.e., the 2DEG layer is terminated by cleaved edge or a vertically etched trench structure. Electrons at the channel edge will then experience net repulsive force from neighboring electrons inside the 2DEG layer. In the case that the charge neutrality is maintained by relatively remote charges (e.g., opposite polarity charges induced across the oxide layer of MOS capacitor), strong in-plane Coulombic repulsion is expected in the local area around the edge of 2DEG, and this can significantly alter the electrostatic potential there (Han & Ihm 2000; Zheng et al. 2004; Mayer 2005). This in-plane Coulombic repulsion has the effect of lowering the vacuum barrier (Figure 1.3) for 2DEG at the edge. Similarly, the energy barrier in the metal side (metal/air interface) is lowered by the 2D positive charges at metal/SiO₂ interface,

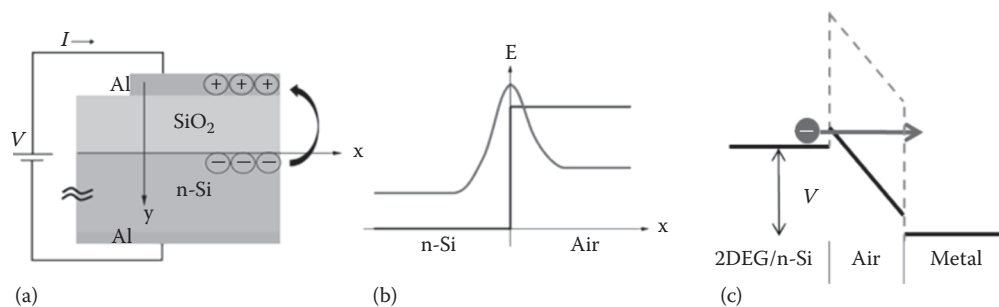


FIGURE 1.3 Energy band diagrams. (a) 2D electron or hole systems induced across the oxide layer of an Al/SiO₂/n-Si MOS capacitor structure. (b) Schematic illustration of electron potential (curved) and energy barrier (step profile) profiles on the plane of the 2DEG layer at the Si/SiO₂ interface. (c) Schematic energy band diagram illustrating the emission of 2DEG under accumulation bias. Coulombic interaction at the edge lowers the energy barriers at cathode (2DEG/n-Si) and anode (metal). 2DEG emits into air at low voltage, travels in the nanovoid channel (air), and is collected by anode.

and the applied capacitor voltage appears mostly across the air gap (i.e., the vertical void channel whose length is defined by the SiO₂ layer thickness).

1.3.1 Calculation of 2DEG Density in a MOS Capacitor Structure

First, we calculate the carrier density of 2DEG induced at SiO₂/Si under forward accumulation bias of a MOS capacitor structure having an infinite lateral extension. In a MOS structure, the space charge density in the semiconductor side can be determined by solving the Poisson equation and is expressed as follows for the case of p-MOS (i.e., on n-Si substrate) (Sze 1981):

$$Q_s = -\epsilon_s E_s = \frac{-\sqrt{2}\epsilon_s}{\beta L_D} \left[(e^{-\beta\phi_s} + \beta\phi_s - 1) + \frac{p_{no}}{n_{no}} (e^{\beta\phi_s} - \beta\phi_s - 1) \right]^{1/2} \quad (1.1)$$

where ϵ_s is the permittivity of the semiconductor and E_s is the electric field at the interface with the oxide layer. ϕ_s is the band bending at the semiconductor/oxide interface, called the surface potential. $\beta = q/kT$, and L_D is the extrinsic Debye length for electrons, given as $\sqrt{\frac{\epsilon_s}{qn_{no}\beta}}$. n_{no} and p_{no} are the equilibrium densities of electrons and holes, respectively.

The applied capacitor voltage (V) appears across mainly three places (neglecting the band bending in the metal side): across the band bending region in semiconductor (ϕ_s), across the oxide layer (V_{ox}), and the flat band voltage (V_{FB}).

$$V = \phi_s + V_{ox} + V_{FB} \quad (1.2)$$

The voltage drop across the oxide layer (V_{ox}) is related to the space charge (Q_s) and oxide capacitance ($C_{ox} = \epsilon_{ox}/d$) as follows:

$$V_{ox} = Q_s/C_{ox}. \quad (1.3)$$

Solving Equations 1.1 to 1.3 simultaneously, the space charge density Q_s can be calculated as a function of applied voltage V .

Figure 1.4 shows the case of a Si p-MOS with $N_D = 1.0 \times 10^{15} \text{ cm}^{-2}$. At $V = 1 \text{ V}$, the MOS is in the accumulation regime, and the space charge density is calculated to be $1 \times 10^{12} \text{ cm}^{-2}$. The same amount of

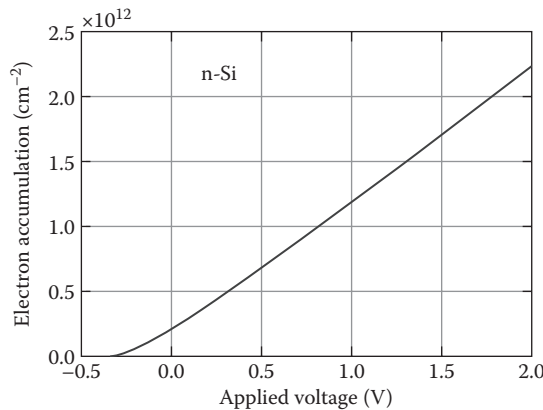


FIGURE 1.4 Accumulation electron density calculated as a function of applied voltage for an Al/SiO₂(23nm)/n-Si capacitor structure.

positive charges accumulates in the metal side. At this bias voltage, the surface potential ϕ_s is 0.21 V and the voltage drop across the oxide layer V_{ox} is 1.11 V.

In this calculation, the following numbers were assumed: the work function of Al, 4.1 eV; electron affinity of Si, 4.15 eV; electron affinity of SiO₂, 0.95 eV; dielectric constant of SiO₂, 3.9; dielectric constant of Si, 11.8 (Lide 2006).

This calculation confirms that the 2DEG density of $\sim 10^{12}$ cm⁻² is easily attainable at low bias voltage (~ 1 V). The average spacing between electrons in the 2DEG is ~ 10 nm, smaller than the oxide thickness (~ 20 nm). This will ensure that the in-plane interaction of 2DEG electrons becomes stronger than the dipole charge interaction across the oxide layer. When the 2DEG layer is terminated at one edge by cleaving the MOS wafer or by vertical etching into SiO₂/Si substrate, the Coulombic repulsion among electrons in 2DEG at the edge is expected to result in overcoming the potential barrier at the Si/air interface. This in-plane Coulombic repulsion will have the effect of lowering the energy barrier at the edge and will enable low-voltage emission of 2DEG into air (Figure 1.3).

1.3.2 Space-Charge-Limited Current Flow of 2DEG in a Nanoscale Void Channel

Nanoscale void channels were fabricated by performing FIB etching of a Si MOS structure (20-nm Al/23-nm SiO₂/n-Si substrate) (Figure 1.5). Square wells ($0.5 \times 0.5 \mu\text{m}^2$, $1 \times 1 \mu\text{m}^2$, and $2 \times 2 \mu\text{m}^2$) were etched to 1 or 2 μm depth. In this vertical structure, the channel length between anode and cathode was precisely determined by the oxide layer thickness (23 nm) and was designed to be smaller than the mean free path of air (~ 60 nm). The current-versus-voltage (I - V) characteristics of the Al/SiO₂/Si structure were measured in dark air ambient at room temperature with a semiconductor parameter analyzer (HP4145B) in conjunction with use of a probe station. Tungsten probes (tip radius of curvature, $\sim 2 \mu\text{m}$) were used in contacting the top and bottom electrodes. The voltage scan was performed with a step size of 0.02 V.

The two-terminal I - V characteristic shows a rectifying behavior with a forward slope of ~ 1.5 and a reverse slope of 0.5–1.0 in the log–log scale plots (Figure 1.5). The channel reveals a forward characteristic when the Al gate is positively biased. This implies that electron emission from the Si side is more efficient than from the metal side at the same bias voltage of opposite polarity. With a $0.5 \times 0.5 \times 1.0 \mu\text{m}^3$

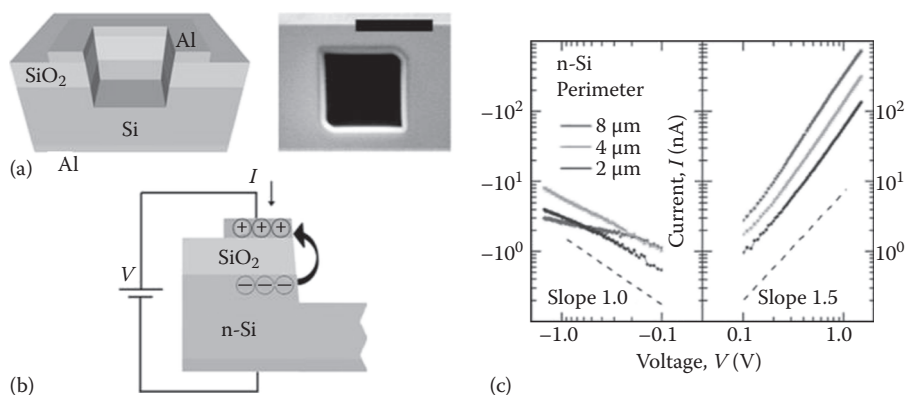


FIGURE 1.5 Ballistic transport of electrons in a nanovoid channel formed in an Al/SiO₂(23nm)/n-Si MOS capacitor structure. (a) Schematic drawing of a nanovoid channel fabricated by FIB etching (left). SEM image of a square well ($1 \times 1 \mu\text{m}^2$) etched to 1 μm depth (right). Scale bar, 1 μm . (b) Schematic of electron emission and transport in a nanovoid channel under forward, accumulation bias. (c) Measured I - V characteristic of square wells (with perimeter of 2, 4, or 8 μm) formed on n-Si. The dashed lines indicate the slope of 1.5 (forward) or 1.0 (reverse). The $V^{1.5}$ voltage dependence corresponds to the CL SCL current flow in vacuum. (Reprinted from Srisonphan, S., Jung, Y.S., Kim, H.K., *Nat. Nanotechnol.*, 7, 504–508, 2012.)

well formed on n-Si, for example, a channel current of 70 nA is observed at +1 V bias, whereas 3 nA is obtained at -1 V bias (Figure 1.5). Comparison of the three different well-size samples (perimeter of 2, 4, or 8 μm) reveals that the forward channel current is proportional to the perimeter of the well, not to the area of the well. This result suggests that electron emission occurs at the edge surface (periphery) on the vertical sidewalls of a well.

In the Al/SiO₂/n-Si MOS capacitor structure, the flat band voltage is -0.32 V, and the MOS at 1 V forward bias is accumulation biased by the amount of 1.32 V. The electron accumulation in Si is estimated to be $1 \times 10^{12} \text{ cm}^{-2}$ at this bias voltage (Figure 1.4). The accumulation electrons form a 2DES, and this layer serves as a reservoir of electrons that would be readily available for emission through the edge under forward bias (the top Al electrode positively biased with respect to n-Si substrate). Because of Coulombic repulsion of electrons around the aperture edge, the 2DEG in Si emits into air and travels toward the edge of 2DHS at Al/SiO₂.

The voltage dependence of electron injection is governed by the capacitor relationship, $Q_e \sim V$. A scattering-free transport of electrons in a void channel converts the potential energy (eV) to kinetic energy ($m^*v^2/2$). The terminal velocity is expressed as $\sqrt{\frac{2eV}{m^*}}$, and the average transit time across the channel has the following voltage dependence: $\tau_{\text{av}} \sim V^{-0.5}$. The voltage dependence of the channel current can then be expressed as $I = Q_e/\tau_{\text{av}} \sim V^{1.5}$, following the Child-Langmuir (CL) three-halves-power law. Here, it should be mentioned that the CL is governed by the space-charge-limited (SCL) emission at cathode. In our case, the electrons injected into air (i.e., nanovoid channel) form a space charge around the anode edge and this space charge field limit the emission of 2DEG at the cathode edge. In reverse bias, part of the bias voltage goes to depletion region formation in Si; therefore, the void-channel section receives less voltage than the accumulation case. This explains the reduced slope (0.5–1.0) in reverse bias (Figure 1.5).

The CL SCL current flow in vacuum is given as follows (Child 1911; Langmuir 1913; Grinberg et al. 1989; Sze 1990):

$$J = \frac{4}{9} \epsilon \sqrt{\frac{2e}{m^*}} \frac{V^{3/2}}{d^2}, \quad (1.4)$$

where ϵ is the permittivity of gap medium, m^* is the effective mass of electron, d is the gap size, and V is the applied voltage.

The SCL current observed in this work demonstrates a scattering-free ballistic transport of electrons across the gap with a negligible barrier height for carrier injection.

To make sure that the observed $V^{3/2}$ dependence is from the electron transport through the air (nanoscale vacuum), not from a surface conduction that might be enabled by possible etch residue or deposit on oxide surface, the same vertical channel structure was fabricated by cleaving a MOS wafer [Al/SiO₂(23nm)/n-Si]. The cleaved samples clearly demonstrate the same rectifying I - V characteristic as the FIB samples (Figure 1.6). The leakage current through the oxide layer, measured before FIB etching, was ~ 20 pA at 2 V bias, far smaller than the channel current level described previously.

In conventional cold-cathode field-emission devices, the electron flow across a metal-nanogap structure usually involves a two-step process: field emission from metal surface, commonly described by the Fowler-Nordheim (FN) theory (Fowler & Nordheim 1928), and a subsequent transport through the gap, governed by the CL SCL current flow (Lau et al. 1994). The CL law assumes zero normal field at cathode surface, whereas the FN emission requires a surface normal field of significant strength (typically ~ 10 V/nm order for metals with work function of 4–5 eV) to enable tunneling emission through the potential barrier at cathode. This implies that the applied voltage initially goes to lowering the potential barrier at the cathode surface, being governed by the FN process. Once a significant amount of electrons are emitted into the gap, the injected electrons in transit form a space charge. As more electrons are injected, the space charge builds up, reducing the field at the cathode surface. At some point, the surface field is reduced to

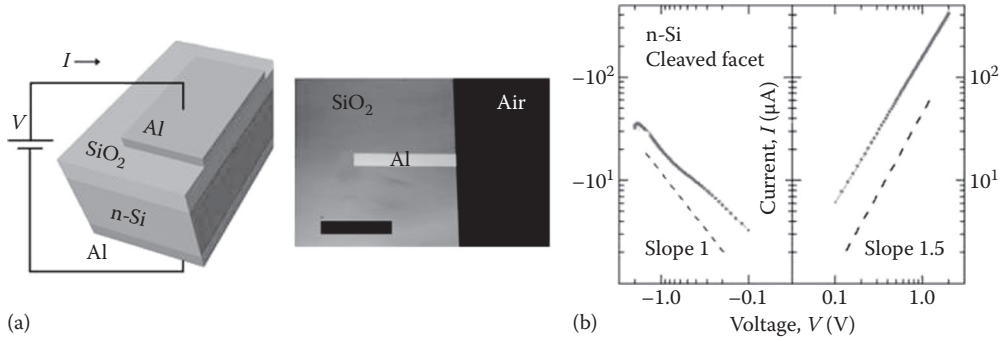


FIGURE 1.6 Nanovoid channel formed on the cleaved facet of an Al/SiO₂(23nm)/n-Si MOS wafer. (a) A schematic of a nanoscale void vertical channel prepared by cleaving a MOS capacitor structure. An Al electrode pad (stripe) was first deposited on an oxidized Si substrate. The MOS wafer was then mechanically cleaved into two pieces, with each cleaved facet comprising cross-sections of MOS layers (left). An optical micrograph of a top view of a cleaved sample with an Al electrode (right: scale bar, 300 μm). (b) Measured I - V characteristic. The cleaved sample clearly demonstrates the same rectifying I - V characteristic (forward slope of 1.5 and reverse slope of 0.5–1.0) as the FIB sample.

zero and the cathode emission, and therefore the channel current, becomes space-charge limited. The transitional relationship between FN and CL regimes in conventional cold-cathode structures is illustrated in Figure 1.7: The FN regime ($JD^2 \propto V^2 e^{-D/V}$) evolves into the CL regime ($JD^2 \propto V^{1.5}$) at large bias. Here, D refers to the gap size. Note that in the conventional cold-cathode surface emission, the transition voltage (from FN to CL) decreases as the gap size is reduced (i.e., as the surface field is increased) (Figure 1.7a and c). In contrast, in the case of edge emission of 2DEG, the energy barriers at cathode and anode are reduced by Coulombic interactions, and this would result in low voltage emission (Figure 1.7b and c).

In the present work, the SCL regime begins to appear at very low voltage (~ 0.5 V), whereas the FN regime is absent in the voltage range tested (< 2 V). The maximum surface field at this onset voltage is estimated to be ~ 0.02 V/nm (i.e., 0.5 V across 23-nm channel length), much smaller than the typical surface field required for FN emission (~ 10 V/nm). This observation is consistent with the earlier reports

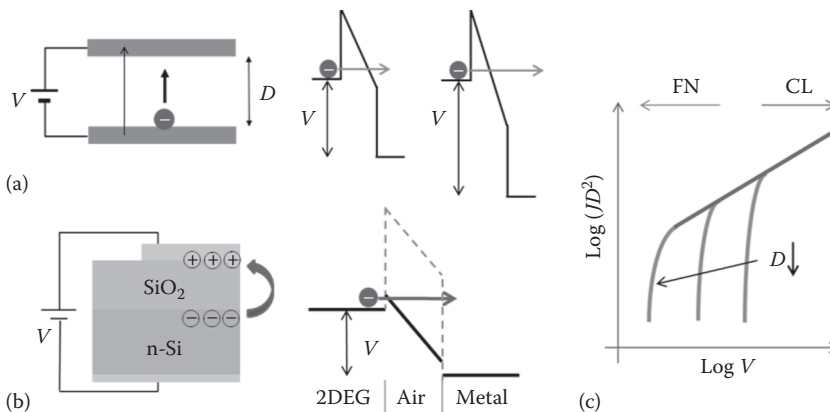


FIGURE 1.7 Evolution of FN emission to CL SCL emission current. (a) Schematic of conventional cold-cathode field emission. The FN tunneling emission requires sufficiently strong field on the cathode surface. The FN regime is governed by $JD^2 \propto V^2 e^{-D/V}$. As the bias voltage is increased, space charges build up. The CL regime emerges at large bias, governed by $JD^2 \propto V^{1.5}$. (b) In the case of edge emission of 2DEG the Coulombic interaction lowers the energy barriers and the CL regime emerges at low voltage. (c) The transitional relationship between FN and CL regimes.

that the barrier height for electrons at cathode edges can be very low for SCL emission (Han & Ihm 2000; Zheng et al. 2004; Mayer 2005). In the 2DES with net accumulation charges, electron emission from cathode edges is virtually thresholdless, enabling very low voltage operation (similar to the negative electron affinity effect) of channel transport with high current density. Similarly, electrons approaching the anode edges will experience Coulombic attraction from the 2D positive charge system formed there, and this will help in capturing electrons into the anode. Unlike conventional cold cathodes (Yang et al. 1991; Mil'shtein et al. 1993; Yun et al. 1999), the nanovoid channel structure also demonstrates good stability and endurance in electron emission (Srisonphan et al. 2012).

1.4 Electron Capture and Transmission at Dark Forward Bias

A graphene membrane was placed on top of a void channel ($500 \text{ nm} \times 500 \text{ nm}$ cross-section; $1 \mu\text{m}$ depth) that was FIB etched or EBL/RIE etched into a SiO_2 (23 nm thickness)/n-Si ($5 \Omega\text{-cm}$ resistivity) substrate (Figure 1.8). A graphene/oxide(or air)/Si (GOS) structure, instead of MOS, was formed by introducing a monolayer graphene as a counterelectrode to the 2DEG layer at the SiO_2/Si interface.

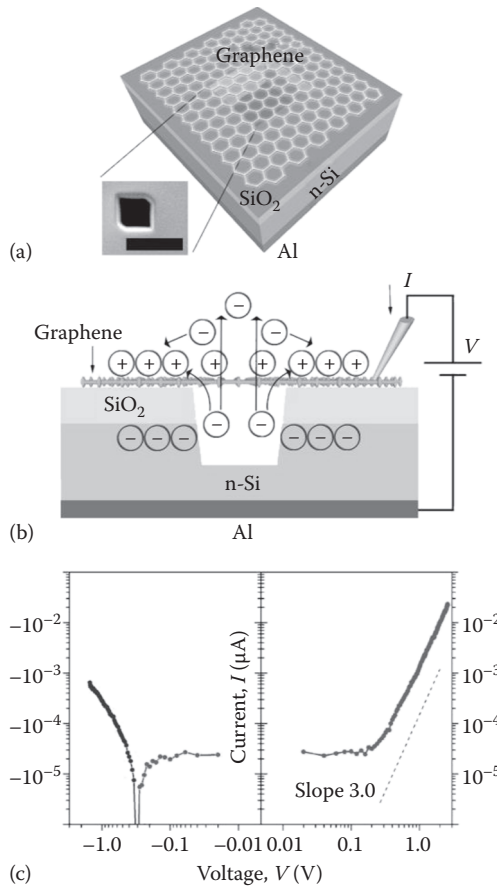


FIGURE 1.8 Transport of very-low-energy ($<3 \text{ eV}$) electrons in a void channel covered with a suspended graphene. (a) Schematic of a graphene/ SiO_2 (23nm)/n-Si structure with a void channel and a top-view SEM image (inset) of a square well ($500 \times 500 \text{ nm}^2$) etched into $1 \mu\text{m}$ depth by FIB. Scale bar, $1 \mu\text{m}$. (b) Schematic of electron emission from the 2DEG at $\text{SiO}_2/\text{n-Si}$ interface and capture/transmission at the graphene anode. (c) Measured I - V characteristic of a void channel (500-nm square well) covered with a monolayer graphene. Note the V^3 dependence ($V > 0.3 \text{ V}$). (Reprinted from Srisonphan, S., Kim, M., Kim, H.K., *Sci. Rep.*, 4, 3764, 2014.)

Here, in the two-terminal mode of operation, the graphene serves as an anode while the n-Si substrate serves as a cathode. Under forward bias (i.e., graphene electrode positively biased with respect to n-Si substrate), a quasi-2DEG (accumulation) develops in the Si side while a 2D hole system (2DHS) forms in the graphene side (Figure 1.8). As a result of Coulombic repulsion of electrons around the aperture edge, the 2DEG in Si emits into air and travels up toward the edge of 2DHS at graphene/SiO₂ interface (Figure 1.8). Some of the incident electrons are captured at the graphene, while others transmit through, forming a space charge region outside the graphene.

It should be noted that in this work, no external collector is employed other than the graphene anode (Spindt 1968; Brodie 1989; Spindt et al. 1991). Therefore, the electrons transmitted through graphene are Coulombically attracted to and collected by the positively biased graphene anode on SiO₂ surface, satisfying the charge neutrality of the overall configuration. The closed-circuit nature (i.e., charge conservation) of this two-terminal operation is confirmed by performing measurements of anode current with the system ground connected to the bottom (cathode) or top (anode) electrode, which demonstrate the same amount of channel current for a given bias voltage (Srisonphan et al. 2014).

1.4.1 Emission and Transport of 2DEG

The dark I - V characteristic was analyzed to understand the emission and transport properties of the quasi-2DEG accommodated at the Si/SiO₂ interface. Figure 1.8 shows a measurement result of the void-channel I - V characteristic. The forward I - V characteristic reveals the V^3 dependence for $V > 0.3$ V. Note that the flat band voltage of this GOS structure is 0.25 V, and an electron accumulation layer begins to develop at around this voltage. At 1 V bias, the channel current is measured to be 1.3 nA. The V^3 regime is called the double injection or injected plasma regime (Lampert & Rose 1961). This corresponds to another type of SCL emission, differing from the CL $V^{1.5}$ dependence or the Mott-Gurney $V^{2.0}$ dependence (Child 1911; Langmuir 1913; Mott & Gurney 1940; Grinberg et al. 1989): The V^3 regime involves bipolar space charges (electrons and holes) injected into a void channel, whereas the latter ones are governed mostly by unipolar space charges (electrons).

In this bipolar space-charge regime (V^3), the cathode emission is governed by the availability of hole charges on graphene (Q_h). The carrier density in graphene has a quadratic dependence on Fermi energy: $n \sim E_F^2$, where E_F refers to the Dirac point (Novoselov et al. 2005; Zhang et al. 2005). In an accumulation-biased graphene/SiO₂/Si capacitor structure, the applied voltage (V) goes to primarily three places: across the oxide layer (V_{ox}), to compensate the flat band voltage (V_{FB}), and to shift the graphene's Fermi level (E_F) (see Section 4.3). As the bias voltage is increased, V_{ox} follows closely ($V_{ox} \sim \alpha V$; $\alpha < 1$). The Fermi level shift can then be expressed as $E_F \sim (V - \alpha V - V_{FB}) \propto (V - V_{offset})$. The hole concentration in graphene will then show a quadratic dependence on voltage ($Q_h \sim V^2$), and the amount of electrons being injected into a channel (Q_e) is expected to show the same voltage dependence ($Q_e \sim Q_h \sim V^2$). With enhanced injection of charge carriers in the channel region, electron transport is expected to show an average velocity that is proportional to the electric field and, therefore, bias voltage: $v_{av} \sim \mu E \sim \mu V/L$. Here, μ is the electron mobility and L is the channel length. The average transit time of electron in the channel is then determined as $\tau_{av} = L/v_{av}$, and the channel current can be expressed as $I = Q_e/\tau_{av} = Q_e v_{av}/L \sim V^3$.

A graphene layer was present in a void channel, and therefore, the availability of holes in the aperture region is expected to affect the space charge field in the channel. In response to electron injection from cathode, for example, the graphene anode brings positive space charges into the void channel by inducing hole charges in the free-standing cover. This has the effect of neutralizing the electron space charges in transit in the channel region (Langmuir & Kingdon 1923; Wilson 1959). With a reduced space charge field on cathode surface, electron emission becomes easier, resulting in a higher channel current with stronger voltage dependence (i.e., V^3 instead of $V^{1.5}$ or $V^{2.0}$).

Besides altering the behavior of SCL emission under forward bias, a free-standing graphene appears to affect the reverse characteristic as well (Figure 1.8). At around -0.3 V, the current level drops to zero, switching the polarity from reverse to forward. Note that bias voltage was swept in the positive direction

from -1.5 V to $+1.5$ V. The early reversal of current flow suggests a discharge of graphene anode around this bias. As the Fermi level is reduced toward the Dirac point, the carrier density of graphene monotonically decreases (Yu et al. 2009). Electrons then evacuate from the graphene at reduced bias, and this exiting (discharging) electron flow has an effect of compensating the reverse leakage (charging) current (Figure 1.8). At some bias point, the two current components cancel each other, causing a zero-current crossing (i.e., a dip in I - V).

To estimate the electron capture efficiency at the edge of graphene anode, the total electron emission from cathode needs to be measured. Here, we refer the electron capture to the directly captured component, not counting the electrons transmitted through graphene and then were collected back by graphene anode via Coulombic attraction. Otherwise, all emitted electrons would be eventually collected/captured by anode (graphene) in this two-terminal mode of operation. In an effort to measure cathode emission, the graphene anode was covered by placing a Ga droplet in the aperture area (Figure 1.9). Here, the Ga droplet size is designed to be much larger than the channel diameter (i.e., $500\ \mu\text{m}$ vs. $500\ \text{nm}$) so that incident electrons are fully blocked by the Ga-covered graphene anode. The forward I - V characteristic clearly reveals the V^3 dependence for $V > 0.1$ V. By placing Ga on top, graphene's work function is expected to decrease slightly by ~ 0.2 eV (Giovannetti et al. 2008). This will then reduce the flat band voltage to ~ 0.12 V, as seen in the earlier onset of steeply rising channel current (Figure 1.9). The V^3 regime of the Ga-covered graphene sample shifted up almost parallel to that of the sample without Ga. This

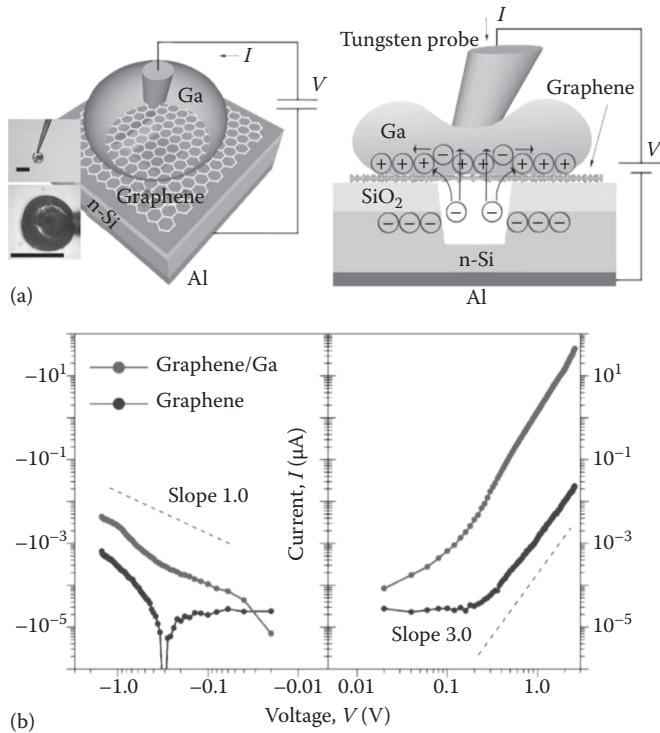


FIGURE 1.9 Electron capture efficiency of a suspended graphene anode. (a) Schematic of electron emission measurement. A Ga droplet is placed on top of the graphene anode covering the entire aperture area (inset: optical micrograph of a Ga droplet attached to a tungsten probe). Scale bars, $500\ \mu\text{m}$. (b) Measured I - V characteristics: with a Ga cover on graphene (top) and without Ga (i.e., graphene only) (bottom). The channel current increased by 1100 times (from $1.3\ \text{nA}$ to $1.4\ \mu\text{A}$ at $1\ \text{V}$ bias) after placing a Ga cover, implying that the electron capture efficiency at a suspended graphene anode is estimated to be $>> \sim 0.1\%$. (Reprinted from Srisonphan, S., Kim, M., Kim, H.K., *Sci. Rep.*, 4, 3764, 2014.)

indicates that the graphene layer underneath Ga still plays the same role of neutralizing electron space charge in the channel as in the case of the graphene-only sample via inducing holes in the suspended area. At 1 V bias, the channel current with graphene/Ga is now measured to be 1.4 μA , a 1.1×10^3 times increase from the current without Ga (1.3 nA).

When assuming all incident electrons are blocked and captured by the graphene/Ga anode, the total electron emission from the cathode equals the measured anode current (1.4 μA). (Here, we note that the reflectivity of very low energy electrons [~ 1 eV] at bulk metal surface is known to be $\sim 10\%$ [Herring & Nichols 1949; Cazaux 2012]. When the reflection effect at the Ga surface is taken into account, the total electron emission from the cathode is expected to be $\sim 10\%$ greater than the measured anode current.) If it is further assumed that the emission current of the graphene/Ga sample remains the same as that of the graphene-only sample, the electron capture efficiency of suspended graphene anode is estimated to be $\sim 0.1\%$ at 1 V bias. By placing a Ga cover on graphene, however, the space charges that might be present in air outside the graphene are expected to be eliminated, and this may further reduce the space charge field in the channel region, thereby enhancing cathode emission. Taking this possible effect into account, we note that the actual cathode emission without Ga might be less than the measured anode current with Ga. Based on this reasoning, the estimated capture efficiency ($\sim 0.1\%$ at 1 V) should be considered as a lower limit.

The 1.4 μA channel current of the graphene/Ga sample at +1 V corresponds to an injection rate of $\sim 10^{13}$ electrons/s at cathode and the same rate of electron capture at Ga-covered graphene anode. The electron transit time in a nanovoid channel (channel length, 23 nm) is estimated to be ~ 100 fs at 1 V bias. This implies that, on average, one electron is in transit inside the void channel. In other words, an average amount of electron space charge is to be of single electron level. A similar amount of hole charges are expected to be induced on the suspended graphene area (500 nm \times 500 nm). The resulting space-charge density in graphene is then estimated to be maximum ~ 4 holes/ μm^2 or $\sim 4 \times 10^8$ holes/ cm^2 . The induction of holes at this level of density is expected to shift the graphene's Fermi level by no more than 0.1 eV at 1 V bias (Das et al. 2008; Xia et al. 2011; Yan et al. 2012). Overall, the result demonstrates graphene's enabling nature of enhancing cathode emission by inducing hole space charge at single electron level, thereby overcoming the CL space charge limit (Child 1911; Langmuir 1913).

Note that the zero-current crossing point in reverse bias (i.e., the dip at -0.3 V in the graphene-only sample) now shifted close to 0 V (~ -0.01 V) with the graphene/Ga sample (Figure 1.9). This is explained by the fact that the Ga-covered graphene has a reduced work function (Fermi level), shifting the discharging of graphene to occur at lower bias. For a given bias voltage, the Fermi level shift at anode might have affected the band bending in the Si side, altering the density of 2DEG at SiO_2/Si and, therefore, cathode emission. To further investigate these possible effects of anode work function change (i.e., graphene Fermi level shift) on emission and capture at 2DES edges, an additional sample structure was prepared and characterized.

1.4.2 Space Charge Neutralization by Suspended Graphene

Without involving graphene, a Ga droplet was directly placed on top of a void-channel-etched $\text{SiO}_2/\text{n-Si}$ substrate, and the resulting I - V characteristic was compared with that of the sample with graphene/Ga (Figure 1.10). Again, the Ga droplet size was designed to be significantly greater than the channel diameter (500 μm vs. 500 nm) so that incident electrons are fully captured.

The forward I - V characteristic reveals the V^2 dependence for $V > 0.1$ V (Figure 1.10). Without space charge neutralization by graphene in the void channel (i.e., without graphene), the voltage dependence of electron injection (Q_e vs. V) follows the capacitor relationship and is expressed as $Q_e \sim V$. With enhanced injection of electrons into the confined space, the electron transport can be expressed in terms of average velocity $v_{\text{av}} \sim \mu E \sim \mu V/L$. The channel current is then determined as $I = Q_e/\tau_{\text{av}} = Q_e v_{\text{av}}/L \sim V^2$. At low bias ($V < 0.8$ V), the sample with Ga-only (top, with slope 2) shows larger current than does the sample with graphene/Ga (bottom). This is explained by the fact that the work function of Ga (4.3 eV)

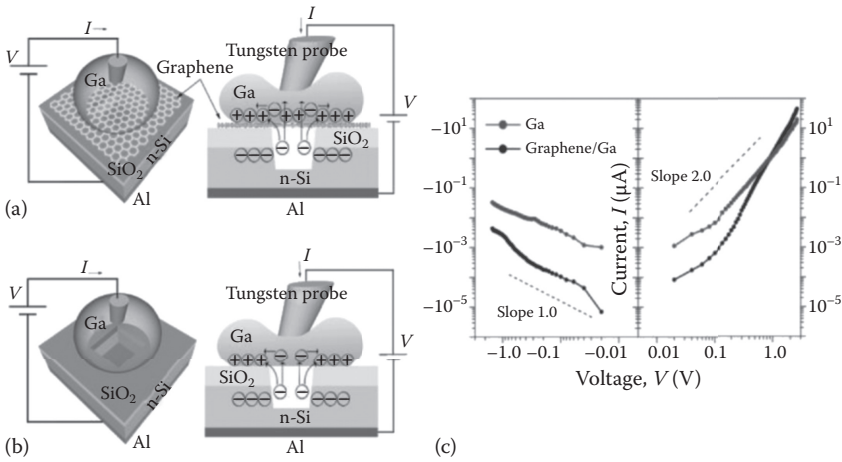


FIGURE 1.10 Enhancement of cathode electron emission by a suspended graphene anode. (a) Schematic of a void channel covered with a Ga droplet as a top cover: with a graphene layer placed underneath a Ga cover. (b) Schematic of a void channel covered with a Ga droplet as a top cover: without graphene underneath. (c) Measured I - V characteristics. The channel current of the sample covered with graphene/Ga (bottom) shows the V^3 voltage dependence, and the current level surpasses the CL SCL current of the sample without graphene (top, with slope 2) at $V > 0.8$ V. (Reprinted from Srisonphan, S., Kim, M., Kim, H.K., *Sci. Rep.*, 4, 3764, 2014.)

is smaller than that of the graphene under Ga (estimated to be 4.43 eV) (Giovannetti et al. 2008), and therefore, accumulation electrons build up more readily at low voltage for the Ga-only sample case. At 0.4 V, for example, the 2DEG density is calculated to be $3.0 \times 10^{11} \text{ cm}^{-2}$ or $1.4 \times 10^{11} \text{ cm}^{-2}$ for the Ga-only or the graphene/Ga sample, respectively (Figure 1.11). The ratio of the two electron densities (2.1) well corresponds to the ratio of channel currents at the same bias (148 nA vs. 53 nA). As bias voltage is increased over the flat band voltage, accumulation electrons build up fast, ensuing electron emission at cathode and space charge build-up in the void channel.

In the graphene/Ga sample case, hole space charges are induced in the suspended graphene area and the double injection regime emerges, as evidenced by a steep rise in channel current at $V > 0.2$ V (Figure 1.9). Note that the V^3 regime of the graphene/Ga sample surpasses the V^2 regime current of the Ga-only

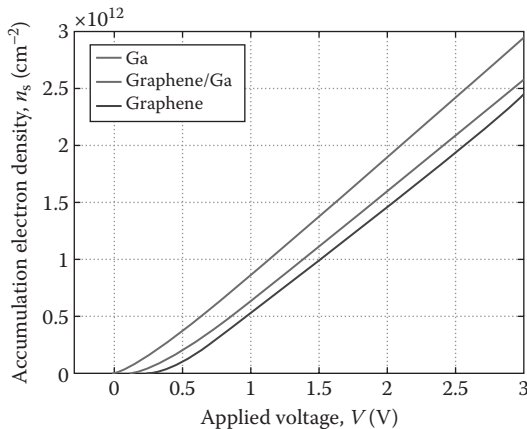


FIGURE 1.11 Accumulation electron density ($n_s = Q_s/q$) in a graphene/SiO₂/Si (GOS) (or MOS) capacitor structure calculated as a function of applied bias voltage V for 0–3 V. Three different cases are shown for top electrode: graphene (bottom); graphene/Ga (middle); Ga (top). SiO₂ thickness, 23 nm; $N_D = 1.0 \times 10^{15} \text{ cm}^{-2}$.

sample at 0.8 V. This hole-charge induction process in graphene has the effect of neutralizing the electron space charges in transit in the channel region (Langmuir & Kingdon 1923; Wilson 1959). With a reduced space charge field on cathode surface, electron emission becomes easier, resulting in higher channel current with stronger voltage dependence (i.e., V^3 instead of $V^{1.5}$ or $V^{2.0}$).

Overall, this comparison clarifies the roles played by graphene in different bias regimes: In low bias, the work function shift at anode alters the 2DEG density at cathode (and therefore, the channel current), whereas in large bias, the suspended graphene directly affects cathode emission by inducing hole space charge in the channel, thereby neutralizing electron space charge.

1.4.3 Calculation of 2DEG Density in Graphene/SiO₂/Si

Here, we calculate the 2DEG density induced at the Si/SiO₂ interface of a capacitor structure formed on a SiO₂/n-Si substrate for the cases of three different electrode materials/configurations: graphene only, graphene/Ga, or Ga only. This comparative study aims at developing a quantitative understanding of how the work function change of top electrode affects the 2DEG density induced in the Si side.

Similar to the MOS capacitor case discussed previously, the bias voltage (V) applied to a graphene/SiO₂/Si (GOS) capacitor structure is expended at mainly three places: the flat band voltage (V_{FB}), across the band bending region in semiconductor (φ_s), and across the oxide layer (V_{ox}).

$$V = V_{FB} + \varphi_s + V_{ox} \quad (1.5)$$

Here, the flat band voltage (V_{FB}) refers to the work function difference of graphene (ϕ_{graphene}) and semiconductor (ϕ_{Si}), expressed as $V_{FB} = \phi_{\text{graphene}} - \phi_{\text{Si}}$.

The work function of intrinsic (undoped) graphene is ~ 4.56 eV (Yu et al. 2009; Yan et al. 2012). Unlike the metal or conventional semiconductor case, graphene offers relatively lower density of states (Luryi 1988). Therefore, the Fermi level of graphene (work function) is not fixed but can shift depending on the bias voltage and, thereby, the level of accommodation of carriers (electrons or holes), i.e., carrier concentration n_s . The Fermi level shift (referring to the Dirac point) can be characterized as

$$\Delta E_F = |v_F| \sqrt{\pi n_s}, \quad (1.6)$$

where v_F is the Fermi velocity, 1.1×10^8 cm/s.

Considering the dependence of flat band voltage on the Fermi level shift in graphene, Equation 1.5 is recast as follows.

$$V = [(\phi_{\text{graphene}} \pm \Delta E_F) - \phi_{\text{Si}}] + \varphi_s + V_{ox} \quad (1.7)$$

Here, the positive sign is for p-type graphene and the negative sign is for the n-type case.

The space charge density (Q_s) in the semiconductor side (n-Si) can be determined by applying the same process as in the MOS case and is expressed as follows.

$$Q_s = -\varepsilon_s E_s = \frac{-\sqrt{2}\varepsilon_s}{\beta L_D} \left[(e^{-\beta\varphi_s} + \beta\varphi_s - 1) + \frac{p_{no}}{n_{no}} (e^{\beta\varphi_s} - \beta\varphi_s - 1) \right]^{1/2} \quad (1.8)$$

Similarly, the voltage drop across the oxide layer (V_{ox}) is related to the space charge in Si (Q_s) and oxide capacitance ($C_{ox} = \varepsilon_{ox}/d$) as follows:

$$V_{ox} = Q_s/C_{ox}. \quad (1.9)$$

Across the oxide layer, the same amount of charges n_s ($= Q_s/q$) (of opposite polarity) appear in the graphene side.

Solving Equations 1.6 to 1.9 simultaneously, the accumulation space charge density Q_s can be calculated as a function of applied voltage V .

Figure 1.11 shows Q_s for V in the range of 0 to 3 V for the structure on n-Si substrate with $N_D = 1.0 \times 10^{15} \text{ cm}^{-3}$. Three different cases were calculated for top electrode on $\text{SiO}_2/\text{n-Si}$ substrate: graphene only, graphene/Ga, and Ga only.

In this calculation, the following numbers were assumed: the work function of Ga, 4.3 eV; electron affinity of Si, 4.15 eV; electron affinity of SiO_2 , 0.95 eV; dielectric constant of SiO_2 , 3.9; dielectric constant of Si, 11.8 (Lide 2006). The work function of Ga-covered graphene is expected to be similar to graphene's, but slightly reduced (to ~ 4.43 eV) because of the contact with Ga, which has a smaller work function than graphene (Giovannetti et al. 2008; Xia et al. 2011).

Now, consider the possible effect of graphene's Fermi level shift on cathode emission and, therefore, on the electron capture efficiency at suspended graphene anode. When a Ga droplet is placed on graphene, the graphene's Fermi level is expected to decrease slightly, from 4.56 eV to 4.43 eV. At low bias, this can make a significant increase in 2DEG density, e.g., at +0.4 V from $5.9 \times 10^{10} \text{ cm}^{-2}$ to $1.4 \times 10^{11} \text{ cm}^{-2}$ after placing Ga. At large bias, however, this effect becomes insignificant, e.g., at +1.0 V bias, the 2DEG density increases from $5.2 \times 10^{11} \text{ cm}^{-2}$ to $6.4 \times 10^{11} \text{ cm}^{-2}$, only a 1.2 times increase (Figure 1.11). The cathode emission of the Ga-covered graphene sample is then estimated to have been affected by the same ratio. Overall, the result confirms good transparency of monolayer graphene to very low energy electrons that up to $\sim 99.9\%$ of incident electrons transmit through a suspended graphene electrode. This high level of electron transparency would be beneficial for low leakage current when a suspended graphene is utilized as a control gate (grid) in vacuum electronic devices.

1.5 Electron Capture and Transmission at Photo Reverse Bias

Under reverse bias, a MOS capacitor structure can support a 2DEG inversion layer at the Si/SiO₂ interface, which forms the basis of Si MOS field-effect-transistor technology (Sze 1981; King et al. 1998). This inversion 2DEG is of minority carriers, thermally generated in Si substrate. Under illumination of light, electron-hole pairs can be generated and separated by depletion field. Photogenerated minority carriers (electrons in p-Si substrate and holes in n-Si) drift to the Si/SiO₂ interface and become confined at the potential well, forming a 2DEG inversion layer. In this study, we investigate a graphene/SiO₂/p-Si (GOS) capacitor structure under reverse bias and optical illumination. The 2DEG at the SiO₂/Si interface is expected to emit into a nanovoid channel, being governed by the same principle as the accumulation 2DEG in a dark, forward-biased graphene/SiO₂/n-Si structure.

A graphene/SiO₂/n-Si structure with a void channel was fabricated by employing EBL, plasma etching, and graphene transfer processes (Figure 1.12). In brief, a vertical trench structure (120–440 nm width, 100–200 nm depth, 1-mm trench length) was formed by plasma RIE of a 23-nm-thick SiO₂-covered (100)-Si substrate (p-type doped with resistivity of 10 Ω-cm). A monolayer graphene (3 mm × 4 mm) was then transferred to the trench-etched substrate.

1.5.1 Photo-Induced 2DEG Inversion Layer

The photo I - V characteristic of graphene/SiO₂/p-Si structure was measured under illumination with a 633-nm laser light (1-mm beam diameter) (Figure 1.12). In reverse bias, the photocurrent saturates at 1.8–4.3 V for 0.1–1.0 mW input power. Under 0.25-mW illumination, the saturation photocurrent is read to be 0.25 mA at 2.7 V. This corresponds to a responsivity of 1.0 A/W and external quantum efficiency (EQE) of 200% (internal quantum efficiency [IQE] of 300%). The dark current is measured to be 1.6–3.6 μA at 2.2–7.0 V, resulting in an on/off current ratio of 225–270 at 1.0 mW input power (Figure 1.12).

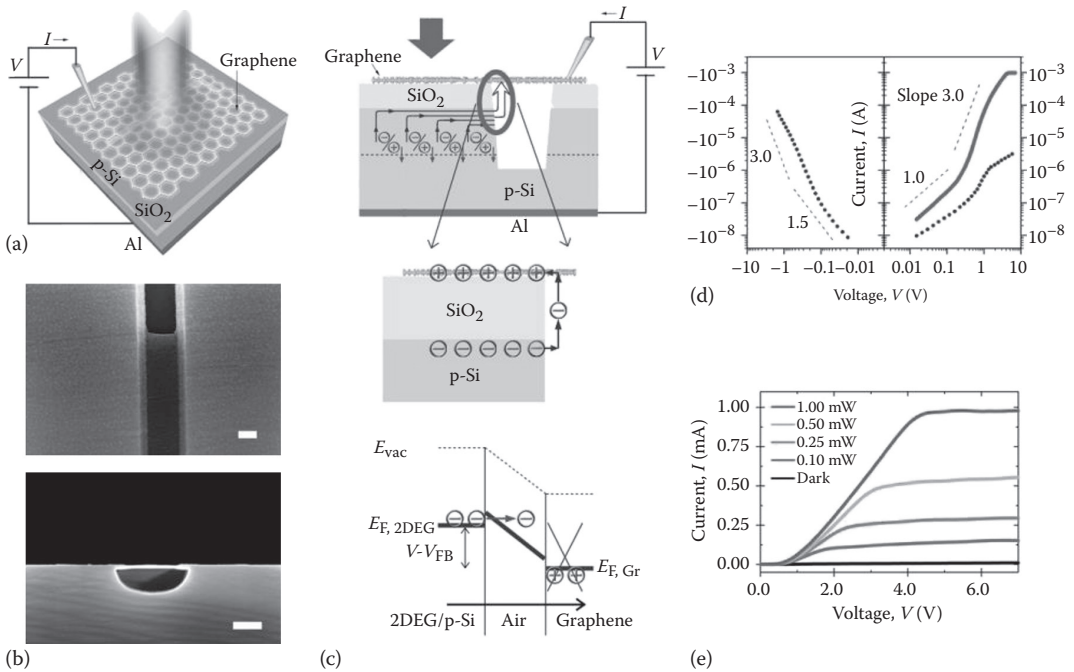


FIGURE 1.12 Emission and transport of photo-induced 2DEG in a graphene/SiO₂(23nm)/p-Si structure with a nanovoid channel under reverse bias. (a) Schematic of a GOS structure with a trench (340–440 nm width, 200 nm depth, 1 mm length) covered by a suspended graphene electrode (3 mm × 4 mm). A laser beam (1 mm diameter) illuminates the graphene electrode. (b) SEM images of monolayer graphene placed on top of a trench: top-view (top) and cross-section (bottom) images. Scale bars, 200 nm. (c) Schematic of photocurrent flow under reverse bias. Photocarriers generated in Si are separated by depletion field: photoelectrons form a 2DEG at Si/SiO₂, while photoholes flow to substrate. The 2DEG flows into/accumulate at the channel edge, while some are exiting into air and traveling toward graphene electrode (top and middle panels). Coulombic repulsion of 2DEG at the channel edge has the effect of lowering the energy barrier at the surface enabling low voltage emission into air. Similarly, the energy barrier in the graphene side is also lowered by the 2DHS in graphene (bottom panel). (d) Measured I - V characteristics: dark- (dotted) and photocurrent (solid) under 1-mW illumination (633 nm wavelength). (e) Measured photo I - V for different input power levels: (from bottom up) black, 0.10 mW, 0.25 mW, 0.50 mW, and 1.00 mW.

The responsivity measured at input power of 0.1 to 1.0 mW remains nearly constant at 0.9–1.1 A/W, demonstrating reasonably good linearity.

The absorption depth of Si is 3.0 μm at 633 nm wavelength. Since a monolayer graphene absorbs only 2.3% of incident light, most photons are absorbed in/near the depletion region (910–940 nm width at 2–5 V reverse bias) (Figure 1.12). The photogenerated carriers are separated by depletion field, and photoelectrons drift to the Si/SiO₂ interface, forming a 2DEG inversion layer. Similar to the dark forward-bias case (Srisonphan et al. 2012), Coulombic repulsion among electrons around the channel edge enables low-voltage emission of 2DEG into air. Emitted electrons travel ballistically in the nanovoid channel. Some of them are captured/collected at the edge of 2DHS induced in the graphene side, while the majority pass through the suspended graphene (Figure 1.12). The transmitted electrons form a space charge outside the suspended graphene. Once a space charge region is established, further transmitting electrons are collected by the graphene electrode on SiO₂. Photoholes separated in the depletion region drift down to the substrate side. Photoelectrons in 2DEG, traveling along the horizontal (longitudinal) direction, accumulate at the channel edge, while some exit through the edge, emitting into air. This

local accumulation of electrons around the edge induces some of the photoholes to be held back near the depletion region boundary. The closed-circuit nature (i.e., charge conservation) of this two-terminal operation with a suspended graphene electrode was confirmed by performing I - V measurements in air or vacuum ($\sim 10^{-6}$ Torr) with the system ground connected to the bottom (cathode) or top (anode), which demonstrate the same amount of channel current for a given bias voltage.

Assuming 1-mW/mm² input power density at 633-nm wavelength and 2.3% absorption in graphene, the photocarrier generation rate in graphene is calculated to be $7.3 \times 10^{15} \text{ s}^{-1} \text{ cm}^{-2}$. Further assuming a minority carrier lifetime of ~ 1 ps (Rana et al. 2009), the photocarrier density in graphene is estimated to be $\sim 7 \times 10^3 \text{ cm}^{-2}$. This number is several orders of magnitude smaller than the 2DEG density in the Si side. This confirms that the photocurrent observed in this work originates from the photocarrier generation and separation occurring in the Si side.

1.5.2 Emission and Transport of Photocarrier 2DEG

Here, we note that the measured photo I - V of reverse-biased p-Si sample reveals the same voltage dependence as the dark forward-biased n-Si case: V^3 dependence of photocurrent at 0.3–1.0 V (Figure 1.12, solid), much faster than the $V^{1.5}$ dependence of CL space-charge-limited current. The 2DEG at SiO₂/Si is balanced by the 2DHS in graphene across the oxide layer, and therefore, the availability of electrons at the channel edge shows the same voltage dependence of hole concentration in graphene: $Q_e \sim Q_h \sim V^2$. Under high-level injection, the electron transport is scattering-limited, and the average velocity is proportional to the electric field, $v_{av} \sim \mu E \sim \mu V/L$. This results in the V^3 dependence of channel current, $I = Q_e/\tau_{av} \sim V^{3.0}$.

The spectral dependence of photocurrent responsivity was characterized in the ultraviolet-to-near-infrared (UV-to-NIR) range (325–1064 nm) at input power of ~ 0.25 mW (Figure 1.13). The IQE shows a three-step cascade profile: an initial rise to 230% level at ~ 850 nm, followed by an increase to 300% level at ~ 650 nm, and a ramp-up to 380% at < 400 nm. At steady state, the saturation photocurrent is balanced by the photocarrier generation in Si. An IQE greater than 100% indicates multiplication of photocarriers (Robbins 1980; Sano & Yoshii 1992; Kolodinski et al. 1993). The spectral dependence of IQE without a carrier multiplication effect is calculated and shown for comparison (Figure 1.13, dashed) (Sze 1981).

The saturation photocurrent (I_{ph}) was read at the knee point (V_{sat}) of photo I - V for ~ 0.25 mW input power (P_{in}). Photocurrent responsivity (I_{ph}/P_{in}) was calculated from the measured photocurrent and input power.

EQE is calculated from

$$\text{EQE} = \frac{I_{ph}/q}{P_{in}/h\nu}. \quad (1.10)$$

IQE is determined from

$$\text{IQE} = \frac{1}{1-R} \frac{I_{ph}/q}{P_{in}/h\nu} = \frac{\text{EQE}}{1-R}. \quad (1.11)$$

Here, R is the reflectance at the sample surface [graphene/SiO₂(23nm)/Si].

The IQE without a carrier multiplication effect (η_{in}) was calculated from (Gärtner 1959)

$$\eta_{in} = 1 - \frac{e^{-\alpha W_D}}{1 + \alpha L_n}. \quad (1.12)$$

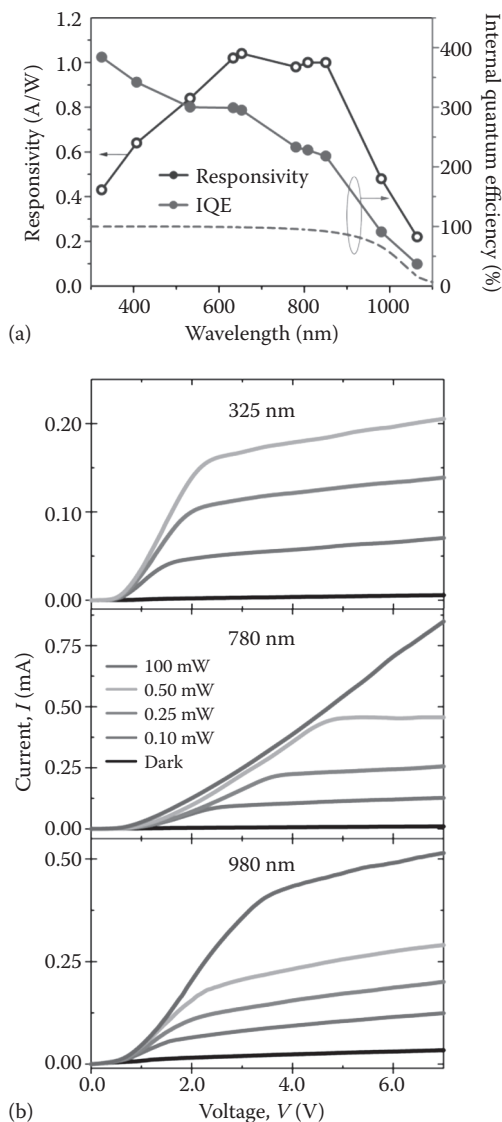


FIGURE 1.13 Spectral dependence of photocurrent responsivity and quantum efficiency. (a) The photo I - V characteristics of a graphene/SiO₂(23nm)/p-Si structure with a trench were measured at 325–1064 nm with input power of ~0.25 mW. The responsivity and IQE values were calculated from the knee points of saturation photocurrents. The spectral dependence reveals a three-step cascade profile with IQE of 220%–380% at <850 nm, implying broadband photocarrier multiplication. The IQE calculated without a multiplication effect is shown for comparison (dashed). (b) Photo I - V characteristics measured at three different wavelengths (325, 780, and 980 nm) with different input power.

Here, α is the absorption coefficient of silicon (Green & Keevers 1995; Lide 2006). L_n is the minority carrier diffusion length (Law et al. 1991). W_D is the dark depletion region width. The EQE without multiplication (η_{ex}) was calculated from $(1 - R)\eta_{in}$.

The three-step-cascade profile observed with the graphene/SiO₂/p-Si structure suggests that different mechanisms are involved in carrier multiplication depending on spectral range. The first regime that covers the NIR (>~800 nm) corresponds to near-band-edge absorption. Since the amount of

above-bandgap excess energy is negligible in this regime, the underlying mechanism is believed to involve a field-assisted process.

The saturation photocurrent is determined by the photocarrier generation rate in Si and is expressed as $q\eta P_{\text{in}}/h\nu$, where q is the electron charge, η is the EQE, P_{in} is the power incident to graphene electrode, and $h\nu$ is the photon energy. For 1-mW illumination with 800-nm light (1-mm beam diameter), the photogeneration rate is calculated to be $2.7 \times 10^{17} \text{ s}^{-1} \text{ cm}^{-2}$. This corresponds to a photocarrier density of $8.2 \times 10^{12} \text{ cm}^{-2}$ when assuming a minority carrier (electron) lifetime of 30 μs in Si (Law et al. 1991). The photogenerated electrons drift to the Si/SiO₂ interface and flow along the 2DEG channel. The channel edge at the trench becomes a bottleneck for continuous flow of electrons (i.e., exit flux into air), since the emission of 2DEG at the edge is limited by the space charge effect in the void channel. Photoelectrons then accumulate at the edge while some return. The local 2DEG density at the bottleneck is expected to stabilize at a certain level because of a negative feedback effect discussed further in the chapter.

Across the oxide layer of the capacitor structure, the graphene side will have an accumulation of positive charge (holes) to the same level as that of net negative charge in Si (Das et al. 2008). The peak hole concentration in graphene is expected to be limited to/stabilized at $\sim 1 \times 10^{13} \text{ cm}^{-2}$. Beyond this level, the electric field in SiO₂ ($> \sim 5 \times 10^6 \text{ V/cm}$) would reach the breakdown regime (Ponomarenko et al. 2013), and carriers (holes) generated by an avalanche process will neutralize the photoelectrons accumulated in Si, reducing the concentration to a stable level. At this level of hole concentration, the Fermi level of graphene is $\sim 0.4 \text{ eV}$ below the Dirac point (Das et al. 2008). A further rise in hole density would lower the graphene's Fermi level and thereby decrease the flat band voltage (V_{FB}) such that the band bending in Si becomes less, lowering the 2DEG density. Overall, this negative feedback effect is expected to limit/stabilize electron accumulation to $\sim 1 \times 10^{13} \text{ cm}^{-2}$ level. In the Si side, the accumulated electrons will attract holes that are being generated in the depletion/neutral region. The photoholes induced by this Coulombic interaction will form a space charge region at the depletion/neutral boundary, altering the field and potential distributions.

1.6 Conclusion

We reviewed the recent progress in investigating suspended graphene's perpendicular interactions with very-low-energy ($< 5 \text{ eV}$) impinging electrons. In this study, a graphene membrane is suspended on top of a nanoscale void channel formed in a SiO₂/Si substrate. In generating a constant flux of very-low-energy electrons, we exploit the phenomenon that a 2DEG induced at the SiO₂/Si interface of a MOS structure can easily emit into air (a void channel whose channel length is smaller than the mean free path) at low voltage ($\sim 1 \text{ V}$) and makes a ballistic transport toward the suspended graphene. Here, the 2DEG is induced by applying dark forward bias (accumulation) or photo reverse bias (inversion). We characterized the emission, capture, and transmission interactions of suspended graphene with the low-energy incident electrons. A small fraction ($> \sim 0.1\%$) of impinging electrons are captured at the edge of 2DHS in graphene, demonstrating good transparency (up to $\sim 99.9\%$) to very-low-energy ($< 5 \text{ eV}$) electrons. While being transmissive, the suspended graphene is found to be highly responsive to impinging electrons. In response to electron injection, a graphene anode induces hole charges in the suspended area, thereby neutralizing electron space charge. This charge compensation dramatically enhances 2DEG emission at cathode to the level far surpassing the CL SCL emission. Besides electron transparency, graphene's ability to overcome the space charge limit in cathode emission offers promising potential for low-voltage, high-current-density nanoscale vacuum electronic devices.

Acknowledgments

This work was supported by the Office of Naval Research (grant no. N00014-1310465) and the National Science Foundation (grant no. ECCS-0925532).

References

- Adam, S. & Sarma, D., "Transport in suspended graphene," *Solid State Commun.* 146 (2008): 356–360.
- Ando, T., Fowler, A. B. & Stern, F., "Electronic properties of two-dimensional systems," *Rev. Mod. Phys.* 54 (1982): 437–625.
- Bao, W., Miao, F., Chen, Z. et al., "Controlled ripple texturing of suspended graphene and ultrathin graphite membranes," *Nat. Nanotechnol.* 4 (2009): 562–566.
- Black, C. T. & Welser, J. J., "Electric-field penetration into metals: Consequences for high-dielectric-constant capacitors," *IEEE Trans. Electron Devices* 46 (1999): 776–780.
- Bolotin, K. I., Sikes, K. J., Jiang, Z. et al., "Ultrahigh electron mobility in suspended graphene," *Solid State Commun.* 146 (2008): 351–355.
- Bolotin, K., Ghahari, F., Shulman, M. D. et al., "Observation of the fractional quantum Hall effect in graphene," *Nature* 462 (2009): 196–199.
- Börrnert, F., Avdoshenko, S. M., Bachmatiuk, A. et al., "Amorphous carbon under 80 kV electron irradiation: A means to make or break graphene," *Adv. Mater.* 24 (2012): 5630–5635.
- Brodie, I., "Physical considerations in vacuum microelectronics devices," *IEEE Trans. Electron Devices* 36 (1989): 2641–2644.
- Bunch, J. S., Verbridge, S. S., Alden, J. S. et al., "Impermeable atomic membranes from graphene sheets," *Nano Lett.* 8 (2008): 2458–2462.
- Cazaux, J., "Reflectivity of very low energy electrons (<10 eV) from solid surfaces: Physical and instrumental aspects," *J. Appl. Phys.* 111 (2012): 064903.
- Chen, J. H., Jang, C., Xiao, S. et al., "Intrinsic and extrinsic performance limits of graphene devices on SiO₂," *Nat. Nanotechnol.* 3 (2008): 206–209.
- Child, C. D., "Discharge from hot CaO," *Phys. Rev.* 32 (1911): 492–511.
- Crespi, V. H., Chopra, N. G., Cohen, M. L. et al., "Anisotropic electron-beam damage and the collapse of carbon nanotubes," *Phys. Rev. B* 54 (1996): 5927–5931.
- Das, A., Pisana, S., Chakraborty, B. et al., "Monitoring dopants by Raman scattering in an electrochemically top-gated graphene transistor," *Nat. Nanotechnol.* 3 (2008): 210–215.
- Du, X., Skachko, I., Barker, A. et al., "Approaching ballistic transport in suspended graphene," *Nat. Nanotechnol.* 3 (2008): 491–495.
- Eisenstein, J. P., Pfeiffer, L. N. & West, K. W., "Negative compressibility of interacting two-dimensional electron and quasiparticle gases," *Phys. Rev. Lett.* 68 (1992): 674–677.
- Fowler, R. H. & Nordheim, L., "Electron emission in intense electric fields," *Proc. Roy. Soc. Lond.* 119 (1928): 173–181.
- Frank, I. W., Tanenbaum, D. M., van der Zande, A. M. et al., "Mechanical properties of suspended graphene sheets," *J. Vac. Sci. Technol. B* 25 (2007): 2558.
- Garaj, S., Hubbard, W., Reina, A. et al., "Graphene as a subnanometre trans-electrode membrane," *Nature* 467 (2010): 190–193.
- Gärtner, W. W., "Depletion-layer photoeffects in semiconductors," *Phys. Rev.* 116 (1959): 84–87.
- Geim, A., "Graphene: Status and prospects," *Science* 324 (2009): 1530–1534.
- Geim, A. K. & Novoselov, K. S., "The rise of graphene," *Nat. Mater.* 6 (2007): 183–191.
- Giovannetti, G., Khomyakov, P. A., Brocks, G. et al., "Doping graphene with metal contacts," *Phys. Rev. Lett.* 101 (2008): 026803.
- Green, M. A. & Keevers, M., "Optical properties of intrinsic silicon at 300 K," *Prog. Photovoltaics* 3 (1995): 189–192.
- Grinberg, A. A., Luryi, S., Pinto, M. R. et al., "Space-charge-limited current in a film," *IEEE Trans. Electron Devices* 36 (1989): 1162–1170.
- Han, S. & Ihm, J., "Role of the localized states in field emission of carbon nanotubes," *Phys. Rev. B* 61 (2000): 9986–9989.

- Han, J.-W., Oh, J. S. & Meyyappan, M., "Vacuum nanoelectronics: Back to the future?—Gate insulated nanoscale vacuum channel transistor," *Appl. Phys. Lett.* 100 (2012): 213505.
- Herring, C. & Nichols, M. H., "Thermionic emission," *Rev. Mod. Phys.* 21 (1949): 185–270.
- Ho, L. H., Micolich, A. P., Hamilton, A. R. et al., "Ground-plane screening of Coulomb interactions in two-dimensional systems: How effectively can one two-dimensional system screen interactions in another," *Phys. Rev. B* 80 (2009): 155412.
- Hu, S., Lozada-Hidalgo, M., Wang, F. C. et al., "Proton transport through one-atom-thick crystals," *Nature* 516 (2014): 227–230.
- Hwang, E. H., Adam, S. & Sarma, D., "Carrier transport in two-dimensional graphene layers," *Phys. Rev. Lett.* 98 (2007): 186806.
- Jernigan, G. G., VanMil, B. L., Tedesco, J. L. et al., "Comparison of epitaxial graphene on Si-face and C-face 4H SiC formed by ultrahigh vacuum and RF furnace production," *Nano Lett.* 9 (2009): 2605–2609.
- Kim, K. S., Jang, H., Lee, S. Y. et al., "Large-scale pattern growth of graphene films for stretchable transparent electrodes," *Nature* 457 (2009): 706–710.
- King, Y.-C., Fujioka, H., Kamoharaet, S. et al., "DC electrical oxide thickness model for quantization of the inversion layer in MOSFETs," *Semicond. Sci. Technol.* 13 (1998): 963–966.
- Koenig, S. P., Boddeti, N. G., Dunn, M. L. et al., "Ultrastrong adhesion of graphene membranes," *Nat. Nanotechnol.* 6 (2011): 543–546.
- Kolodinski, S., Werner, J. H., Wittchen, T. et al., "Quantum efficiencies exceeding unity due to impact ionization in silicon solar cells," *Appl. Phys. Lett.* 63 (1993): 2405–2407.
- Kotov, V. N., Uchoa, B., Vitor, M. et al., "Electron–electron interactions in graphene: Current status and perspectives," *Rev. Mod. Phys.* 84 (2012): 1067–1125.
- Krasheninnikov, A. V. & Nordlund, K., "Ion and electron irradiation-induced effects in nanostructured materials," *J. Appl. Phys.* 107 (2010): 071301.
- Kreuzer, H. J., Nakamura, K., Wierzbicki, A. et al., "Theory of the point source electron microscope," *Ultramicroscopy* 45 (1992): 381–403.
- Kuhr, J.-C. & Fitting, H.-J., "Monte Carlo simulation of electron emission from solids," *J. Electr. Spectr. Rel. Phenom.* 105 (1999): 257–273.
- Lampert, M. A. & Rose, A., "Volume-controlled, two-carrier currents in solids: The injected plasma case," *Phys. Rev.* 121 (1961): 26–37.
- Landau, L. D. & Lifshitz, E. M., *Statistical Physics*, Part I, Sections 137 and 138 (Pergamon, Oxford, 1980).
- Langmuir, I., "The effect of space charge and residual gases on thermionic currents in high vacuum," *Phys. Rev.* 2 (1913): 450–486.
- Langmuir, I. & Kingdon, K. H., "Thermionic effects caused by alkali vapors in vacuum tubes," *Science* 57 (1923): 58–60.
- Lau, Y. Y., Liu, Y. & Parker, R. K., "Electron emission: From the Fowler–Nordheim relation to the Child–Langmuir law," *Phys. Plasmas* 1 (1994): 2082–2085.
- Law, M. E., Solley, E., Liyang, M. et al., "Self-consistent model of minority-carrier lifetime, diffusion length, and mobility," *IEEE Electron Device Lett.* 12 (1991): 401–403.
- Lee, C., Wei, X., Kysar, J. W. & Hone, J., "Measurement of the elastic properties and intrinsic strength of monolayer graphene," *Science* 321 (2008): 385–388.
- Li, X., An, J., Kim, S. et al., "Large-area synthesis of high-quality and uniform graphene films on copper foils," *Science* 324 (2009): 1312–1314.
- Li, L., Richter, C., Paetel, S. et al., "Very large capacitance enhancement in a two-dimensional electron system," *Science* 332 (2011): 825–828.
- Li, C., Cole, M. T., Lei, W. et al., "Highly electron transparent graphene for field emission triode gates," *Adv. Funct. Mater.* 24 (2014): 1218–1227.
- Lide, D. R., ed., *CRC Handbook of Chemistry and Physics*, 87th ed. (CRC Press, Boca Raton, FL, 2006).

- Liu, L., Ryu, S., Tomasik, M. R. et al., "Graphene oxidation: Thickness-dependent etching and strong chemical doping," *Nano Lett.* 8 (2008): 1965–1970.
- Luryi, S., "Quantum capacitance devices," *Appl. Phys. Lett.* 52 (1988): 501–503.
- Mattevi, C., Kim, H. & Chhowalla, M., "A review of chemical vapor deposition of graphene on copper," *J. Mater. Chem.* 21 (2011): 3324–3334.
- Mayer, A., "Polarization of metallic carbon nanotubes from a model that includes both net charges and dipoles," *Phys. Rev. B* 71 (2005): 235333.
- Mead, C. A., "Anomalous capacitance of thin dielectric structures," *Phys. Rev. Lett.* 6 (1961): 545–546.
- Mermin, N. D., "Crystalline order in two dimensions," *Phys. Rev.* 176 (1968): 250–254.
- Meyer, J. C., Geim, A. K. & Katsnelson, M. I., "The structure of suspended graphene sheets," *Nature* 446 (2007): 60–63.
- Mil'shtein, S., Paludi, Jr., C. A., Chau, P. et al., "Perspectives and limitations of vacuum microtubes," *J. Vac. Sci. Technol. A* 11 (1993): 3126–3129.
- Morin, P., Pitaval, M. & Vicario, E., "Low energy off-axis holography in electron microscopy," *Phys. Rev. Lett.* 76 (1996): 3979–3982.
- Morozov, S. V., Novoselov, K. S., Katsnelson, M. I. et al., "Giant intrinsic carrier mobilities in graphene and its bilayer," *Phys. Rev. Lett.* 100 (2008): 016602.
- Mott, N. F. & Gurney, R. W., *Electronic Processes in Ionic Crystals* (Oxford Univ Press, New York, 1940).
- Müllerová, I., Hovorka, M., Hanzlíková, R. et al., "Very low energy scanning electron microscopy of free-standing ultrathin films," *Mater. Trans.* 51 (2010): 265–270.
- Mutus, J. Y., Livadaru, L., Robinson, J. T. et al., "Low-energy electron point projection microscopy of suspended graphene, the ultimate 'microscope slide,'" *New J. Phys.* 13 (2011): 063011.
- Neto, A. H. C., Guinea, F., Peres, N. M. R. et al., "The electronic properties of graphene," *Rev. Mod. Phys.* 81 (2009): 109–162.
- Novoselov, K. S., Geim, A. K., Morozov, S. V. et al., "Electric field effect in atomically thin carbon films," *Science* 306 (2004): 666–669.
- Novoselov, K. S., Geim, A. K., Morozov, S. V. et al., "Two-dimensional gas of massless Dirac fermions in graphene," *Nature* 438 (2005): 197–200.
- Ponomarenko, L. A., Gorbachev, R. V., Yu, G. L. et al., "Cloning of Dirac fermions in graphene superlattices," *Nature* 497 (2013): 594–597.
- Rana, F., George, P. A., Strait, J. H., Dawlaty, J., Shivaraman, S., Chandrashekar, M. & Spencer, M. G., "Carrier recombination and generation rates for intravalley and intervalley phonon scattering in graphene," *Phys. Rev. B* 79 (2009): 115447.
- Robbins, D. J., "Aspects of the theory of impact ionization in semiconductors (I)," *Phys. Stat. Sol. B* 97 (1980): 9–50.
- Sano, N. & Yoshii, A., "Impact-ionization theory consistent with a realistic band structure of silicon," *Phys. Rev. B* 45 (1992): 4171–4180.
- Schedin, F., Geim, A. K., Morozov, S. V. et al., "Detection of individual gas molecules adsorbed on graphene," *Nat. Mater.* 6 (2007): 652–655.
- Shivaraman, S., Barton, R. A., Yu, X. et al., "Free-standing epitaxial graphene," *Nano Lett.* 9 (2009): 3100–3105.
- Spindt, C. A., "A thin-film field-emission cathode," *J. Appl. Phys.* 39 (1968): 3504–3505.
- Spindt, C. A., Brodie, I., Humphrey, L. et al., "Physical properties of thin-film field emission cathodes with molybdenum cones," *J. Appl. Phys.* 47 (1976): 5248–5263.
- Spindt, C. A., Holland, C. E., Rosengreen, A. et al., "Field-emitter arrays for vacuum microelectronics," *IEEE Trans. Electron Devices* 38 (1991): 2355–2363.
- Srisonphan, S., Jung, Y. S. & Kim, H. K., "Metal-oxide-semiconductor field-effect transistor with a vacuum channel," *Nat. Nanotechnol.* 7 (2012): 504–508.
- Srisonphan, S., Kim, M. & Kim, H. K., "Space charge neutralization by electron-transparent suspended graphene," *Sci. Rep.* 4 (2014): 3764.

- Stoner, B. R. & Glass, J. T., "Nanoelectronics: Nothing is like a vacuum," *Nat. Nanotechnol.* 7 (2012): 485–487.
- Suk, J. W., Kitt, A., Magnuson, C. W. et al., "Transfer of CVD-grown monolayer graphene onto arbitrary substrates," *ACS Nano* 5 (2011): 6916–6924.
- Sze, S. M., *Physics of Semiconductor Devices*, 2nd ed. (Wiley, New York, 1981).
- Sze, S. M. ed., *High-Speed Semiconductor Devices* (Wiley, New York, 1990).
- Toriumi, A., Yoshimi, M., Iwase, M. et al., "Experimental determination of finite inversion layer thickness in thin gate oxide MOSFETs," *Surf. Sci.* 170 (1986): 363–369.
- Wilson, V. C., "Conversion of heat to electricity by thermionic emission," *J. Appl. Phys.* 30 (1959): 475–481.
- Xia, F., Perebeinos, V., Lin, Y.-M. et al., "The origins and limits of metal-graphene junction resistance," *Nat. Nanotechnol.* 6 (2011): 179–183.
- Yan, R., Zhang, Q., Li, W. et al., "Determination of graphene work function and graphene-insulator-semiconductor band alignment by internal photoemission spectroscopy," *Appl. Phys. Lett.* 101 (2012): 022105.
- Yang, G., Chen, K. K. & Marcus, R. B., "Electron field emission through a very thin oxide layer," *IEEE Trans. Electron Devices* 38 (1991): 2373–2376.
- Yu, Y.-J., Zhao, Y., Ryu, S. et al., "Tuning the graphene work function by electric field effect," *Nano Lett.* 9 (2009): 3430–3434.
- Yun, M., Turner, A., Roedel, R. J. et al., "Novel lateral field emission device fabricated on silicon-on-insulator material," *J. Vac. Sci. Technol. B* 17 (1999): 1561–1566.
- Zhang, Y., Tan, Y.-W., Stormer, H. L. et al., "Experimental observation of the quantum Hall effect and Berry's phase in graphene," *Nature* 438 (2005): 201–204.
- Zheng, X., Chen, G., Li, Z. et al., "Quantum-mechanical investigation of field-emission mechanism of a micrometer-long single-walled carbon nanotube," *Phys. Rev. Lett.* 92 (2004): 106803.

This page intentionally left blank

2

Graphene Quantum Dots

	2.1	Introduction	30
	2.2	Band Structure of Graphene and Bilayer Graphene.....	31
	2.3	Electronic and Optical Properties of Graphene and Bilayer Graphene Quantum Dots (QDs)	33
		Graphene in Reduced Dimensions • Relevant Energy Scales • Optical Properties	
	2.4	Fabrication of Graphene Nanostructures	37
		Top-Down Approach • Bottom-Up Approach	
	2.5	Graphene Single-Electron Transistors and QDs.....	40
		GNRs and Nanostructures • Single-Electron Transistors • QDs in Width-Modulated Nanostructures • Charge Detection • Spin States in a Graphene QD • Charge Relaxation in Graphene QDs • Gate-Defined QDs in GNRs • QDs Defined by Anodic Oxidation • QDs on Hexagonal Boron Nitride	
Christian Volk	2.6	Bilayer Graphene QDs.....	53
		Soft Confinement of QDs in Bilayer Graphene	
Christoph Neumann	2.7	DQDs in Graphene and Bilayer Graphene	54
Stephan Engels		DQDs in Graphene • High-Frequency Gate Manipulation • DQDs in Bilayer Graphene	
Alexander Epping	2.8	Applications of Graphene QDs.....	59
Christoph Stampfer	2.9	Conclusions and Outlook.....	59
		References.....	59

Abstract

This chapter reviews experiments on graphene and bilayer graphene quantum dot devices. First, a brief theoretical background is given. The electronic and optical properties of graphene QDs are explained, and the differences from extended graphene sheets are emphasized.

The most common fabrication technique is based on micromechanical exfoliation of individual graphene flakes from bulk graphite followed by plasma etching the desired shape. Carving width modulated nanoribbons out of graphene flakes, it has been possible to realize single electron transistors, quantum dots, and double quantum dots. Following a bottom-up approach, graphene QDs can either be fabricated by ruthenium-catalyzed C60 transformation, by hydrothermal or electrochemical strategies from graphene oxide, or by wet chemical oxidization and cutting of micrometer-sized carbon fibers. These types of graphene QDs are used in optical and biological experiments.

The transport properties of graphene nanoribbons are summarized. They allow opening a band-gap in graphene by lateral confinement and thus serve as building blocks for many graphene quantum devices. Graphene quantum dots have intensively been studied in low-temperature DC measurements. Coulomb blockade and excited state spectra have been investigated in graphene quantum

dots. Graphene nanoribbon-based charge sensors are commonly used to detect charging events in regimes where the current through the quantum dots is below the detection limit. Furthermore, time-resolved charge detection on a graphene quantum dots has been demonstrated. In magnetic field-dependent measurements, it was possible to determine spin-filing sequences and the g-factor in graphene quantum dots. The relaxation dynamics of excited states in quantum dots is addressed by pulsed gate spectroscopy. Measurements of transient currents through electronic excited states give an estimate for a lower bound for charge relaxation times on the order of 60–100 ns.

As the quality of graphene devices is regarded to be limited by disorder induced by surface potentials of the host substrate and edge states, alternative fabrication techniques have been investigated. Local anodic oxidation avoids the use of lithography and plasma etching and can thus potentially reduce the influence of edge disorder. Spin states have been investigated in devices built following this technique. To cope with the problem of substrate-induced disorder, graphene quantum dots on hexagonal boron nitride (hBN) have been investigated. A competitive study of devices on hBN and SiO₂ has shown a significant reduction of the influence of surface-induced disorder.

Bilayer graphene is of special interest as it allows to open a bandgap by applying perpendicular electric fields. This approach has been used to realize quantum dots by soft confinement. Bilayer graphene quantum dots in suspended flakes and in hBN/bilayer graphene/hBN heterostructures have been studied.

The device concepts known from quantum dots have been extended to realize double quantum dots. Excited state spectra, the gate control of the mutual capacitive coupling and the interdot tunnel coupling, have been studied. By pulsed gate control on a double quantum dot, a gigahertz charge pump has been demonstrated. Studies on a bilayer graphene double quantum dot have proven that the excited state level spacing in bilayer graphene is constant in contrast to single-layer graphene. A magnetic field dependency of excited states in agreement with Zeeman splitting has been observed.

2.1 Introduction

Quantum dots (QDs) allow a controlled investigation and manipulation of individual quantum systems. They are in particular interesting as promising hosts for spin qubits (Loss and DiVincenzo 1998). These are reasons why QDs have been intensively investigated in different material systems over the past years. So far, most progress has been made in QDs in two-dimensional (2D) electron gases, especially in GaAs-based heterostructures (Elzermann et al. 2003; Hanson 2005; Johnson et al. 2005; Petta et al. 2005; Koppens et al. 2006; Nowack et al. 2011), and elementary spin-qubit operations have been demonstrated.

However, these systems suffer from limited spin decoherence times originating from spin-orbit and hyperfine interactions (Khaetskii et al. 2002). Ways to cope with this issue have been explored, e.g., by polarizing the nuclear spin bath (Bluhm et al. 2010). To minimize the influence of nuclear spins, alternative materials are of great interest, especially group IV elements. Spin relaxation has been measured, e.g., in Ge/Si nanowire qubits (Hu et al. 2011) and in silicon QDs (Yang et al. 2013). Recently, electron spin resonance has been demonstrated in a Si/SiGe spin qubit, with decay timescales significantly larger compared with III/V QDs (Kawakami et al. 2014). One way to further reduce the influence of nuclear spins is the use of isotopically purified silicon.

Among the group IV elements, carbon materials are an interesting alternative. The spin-orbit interaction is small because of the low mass of the nucleus (Huertas-Hernando et al. 2006; Min et al. 2006). The hyperfine interaction is weak, as 99% of natural carbon is the isotope C¹², which has zero nuclear spin (Trauzettel et al. 2007). A valley-spin qubit in a carbon nanotube (CNT) has been studied by Hahn echo measurements (Laird et al. 2013). It is predicted that spin-qubits in graphene feature long coherence times (Trauzettel et al. 2007).

Despite the advantages concerning hyperfine and spin-orbit interaction, graphene has a significant drawback. Because of the absence of a bandgap and the pseudorelativistic Klein tunneling effect, it is challenging to confine electrons (Katsnelson et al. 2006; Castro Neto et al. 2009; Das Sarma et al. 2011).

A lot of effort has been spent so far to overcome this limitation. Most approaches are based on carving nanostructures out of graphene sheets. It has been shown that an energy gap will be opened in graphene nanoribbons (GNRs). Single-electron transistors (SETs), QDs, and double QDs (DQDs) have successfully been fabricated either by etching width-modulated nanostructures (Ponomarenko et al. 2008; Stampfer et al. 2008b; Güttinger et al. 2009; Moriyama et al. 2009; Molitor et al. 2009b; Wang et al. 2010; Volk et al. 2011; Connolly et al. 2013; Volk et al. 2013; Engels et al. 2013b) or by electrostatic confinement of electrons in nanoribbons using gate electrodes (Liu et al. 2009, 2010). Another technique defines the nanostructures by local anodic oxidation (Neubeck et al. 2010; Puddy et al. 2013). Recently, the confinement of electrons by magnetic fields has been demonstrated (Moriyama et al. 2014). In addition, bilayer graphene offers the possibility for soft confinement of electrons by applying perpendicular electric fields (Allen et al. 2012; Goossens et al. 2012b).

Graphene QDs are not only investigated in electronic transport experiments but also their optical properties are explored, e.g., by photoluminescence (PL) and PL excitation (PLE) (Kim et al. 2012; Peng et al. 2012). Although no optical luminescence is observed in extended graphene sheets, the size-dependent confinement gap in graphene QDs results in size-dependent (and hence controllable) emission and absorption spectra, which makes graphene QDs promising for optoelectronic and bioimaging applications.

2.2 Band Structure of Graphene and Bilayer Graphene

Graphene is a 2D crystal where neighboring carbon atoms form strong covalent sp^2 σ -bonds with a binding angle of 120° , resulting in a hexagonal crystal structure that can be regarded as a trigonal lattice with two atoms per unit cell. The carbon-carbon bond length measures $a_0 = 1.42 \text{ \AA}$ (see Figure 2.1a). The remaining p_z orbitals of the carbon atoms give rise to the so-called π -bands responsible for the electronic properties of graphene.

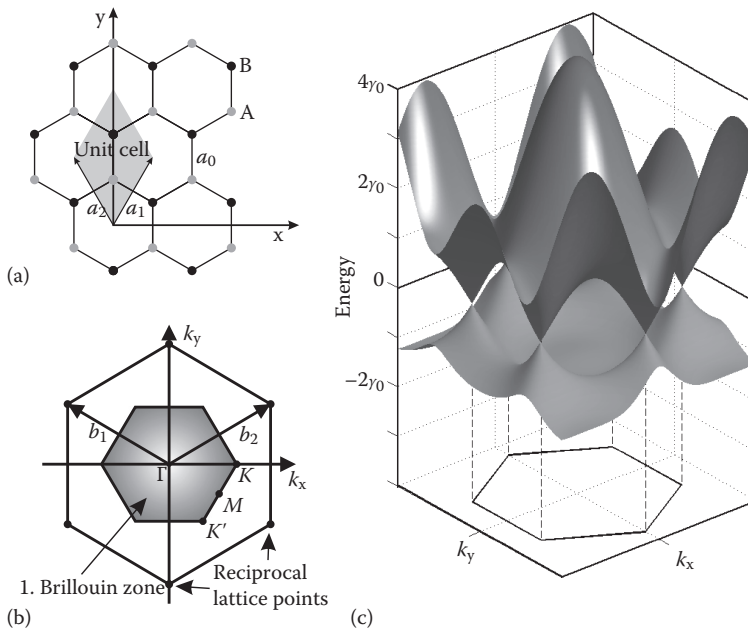


FIGURE 2.1 Crystal structure and band structure of single-layer graphene. (a) Crystal structure of graphene in real space. The colors distinguish between the A and B sublattice. The unit cell is shaded in gray. (b) Reciprocal lattice of graphene. The first Brillouin zone is highlighted, including the high symmetry points Γ , M , K , and K' . (c) Nearest-neighbor tight-binding band structure calculation (cf. Equation 2.1). The π - and π^* -bands touch at the K - and K' -points.

The first Brillouin zone shows a hexagonal symmetry reminding of the graphene crystal structure in real space (see Figure 2.1b). The two inequivalent corners of the Brillouin zone are $\mathbf{K} = (2\pi/3a_0)(1, \sqrt{3})$ and $\mathbf{K}' = (2\pi/3a_0)(1, -\sqrt{3})$.

The electronic band structure can be derived following a tight-binding approach (Wallace 1947). Taking into account both nearest-neighbor and next-nearest-neighbor hopping terms results in a band structure expressed by the relation (Castro Neto et al. 2009; Das Sarma et al. 2011; Katsnelson et al. 2012).

$$E_{\pm}(\mathbf{k}) = \pm\gamma_0\sqrt{3+f(\mathbf{k})} - \gamma'_0 f(\mathbf{k}), \quad (2.1)$$

with

$$f(\mathbf{k}) = f(k_x, k_y) = 2\cos(\sqrt{3}k_y a_0) + 4\cos(\sqrt{3}/2k_y a_0)\cos(3/2k_x a_0). \quad (2.2)$$

The nearest-neighbor hopping energy measures $\gamma_0 \approx 2.8$ eV. According to ab initio calculations, the next-nearest-neighbor hopping energy γ'_0 has been found to be on the order of $-0.02\gamma_0$ to $-0.2\gamma_0$ (Reich et al. 2002). The positive and negative branches of the dispersion relation correspond to the π - and π^* -band, respectively. Finite γ'_0 breaks the electron hole symmetry. A detailed calculation can be found, e.g., in review articles by Castro Neto et al. (2009) and Das Sarma et al. (2011). Figure 2.1c shows the band structure for $\gamma_0 = 2.8$ eV and $\gamma'_0 = -0.2\gamma_0$.

At the center of the Brillouin zone, the Γ -point, the conduction and valence bands are separated by $6\gamma_0 \approx 17$ eV, whereas the bands touch at the K-points of the Brillouin zone, making graphene a semimetal. In transport measurements, usually, only energies close to the Fermi energy are accessible; thus, only the dispersion relation close to the charge neutrality point is relevant. In this regime, the dispersion relation can be linearized around \mathbf{K} as $E_{\pm}(\mathbf{k}) = \pm\hbar v_F |\mathbf{k}|$, where v_F is the Fermi velocity $3\gamma_0 a_0 / 2\hbar \approx 10^6$ m/s (Wallace 1947; Katsnelson et al. 2006; Neto et al. 2006; Katsnelson and Novoselov 2007). As the dispersion relation takes the form of the one valid for massless relativistic particles ($E = cp = \hbar c |k|$, where c is the speed of light), the K-points are called Dirac points. The density of states is given by $D(E) = 2|E| / (\pi\hbar^2 v_F^2)$ in contrast to conventional 2D electron gases (2DEGs), where it is independent of energy.

Bilayer graphene is formed by two graphene sheets Bernal stacked on top of each other. In close analogy to single-layer graphene, the band structure can be obtained by a tight-binding approach taking into account intralayer and interlayer hopping (γ_0, γ_1) (cf. Figure 2.2).

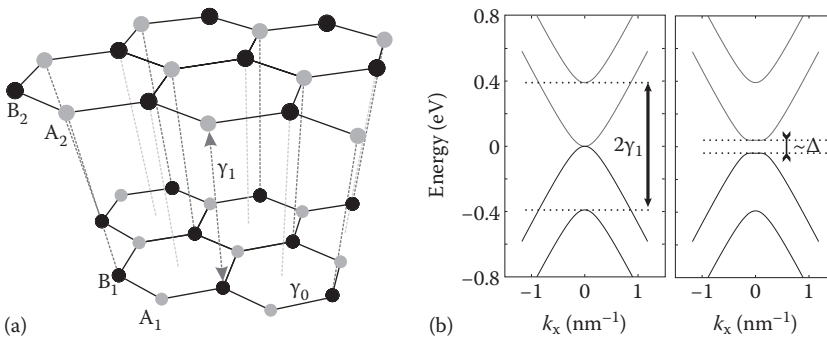


FIGURE 2.2 Crystal structure and band structure of bilayer graphene. (a) Crystal structure of bilayer graphene. The interlayer distance measures $c_0 = 3.35$ Å, the intralayer hopping energy $\gamma_0 \approx 2.8$ eV, and the interlayer hopping energy $\gamma_1 \approx 0.4$ eV. (From Du, X. et al., *Nature*, 462, 192–195, 2009.) The latter describes the coupling of B_1 atoms in the lower layer and A_2 atoms in the upper layer. (b) Band structure in the absence of an external electric field and the presence of a perpendicular external electric field leading to a potential difference of $\Delta = 80$ mV, which breaks the lattice symmetry and thus leads to a bandgap opening.

The energy dispersion relation around the K-point is given by

$$E_{\pm}(k) = \pm \left(\hbar^2 v_F^2 k^2 + \gamma_1^2 / 2 \pm \sqrt{\gamma_1^4 / 4 + \gamma_1^2 \hbar^2 v_F^2 k^2} \right)^{1/2}. \quad (2.3)$$

The sign in front of the inner square root distinguishes between the first and second energy subbands, which are split by $2\gamma_1 \approx 0.78$ eV (Brandt et al. 1988; Dresselhaus and Dresselhaus 2002; McCann et al. 2006; Castro Neto et al. 2009; Das Sarma et al. 2011).

In the limit of low momenta ($k \ll \gamma_1 / (2\hbar v_F)$), the dispersion relation simplifies to $E_{\pm}(k) = \pm \hbar^2 v_F^2 k^2 / \gamma_1$, describing a parabolic dispersion relation. As a consequence, the quasiparticles have a finite effective mass $m^* = \gamma_1 / 2v_F^2$ and the density of states is constant: $D(E) = \gamma_1 / (\pi \hbar^2 v_F^2)$. At large k , the dispersion relation converges toward the linear one known from single-layer graphene.

Interestingly, bilayer graphene allows the opening of a bandgap by applying a perpendicular electric field. Taking into account this effect, the energy dispersion relation reads as

$$E_{\pm}(k) = \pm \left(\Delta^2 / 4 + \hbar^2 v_F^2 k^2 + \gamma_1^2 / 2 \pm \sqrt{\gamma_1^4 / 4 + (\gamma_1^2 + \Delta^2) \hbar^2 v_F^2 k^2} \right)^{1/2}, \quad (2.4)$$

where Δ is a measure for the potential energy difference of the two graphene layers (Brandt et al. 1988; McCann et al. 2006; Das Sarma et al. 2011; Katsnelson 2012; Castro Neto et al. 2009). As long as Δ is small compared to γ_0 , the dispersion relation remains parabolic around the K-point, while at larger Δ , the curve takes the typical “mexican hat”-like shape with a minimum bandgap of $\Delta - \Delta^2 / 2\gamma_1^2$. Figure 2.2b compares the band structure with and without an applied electric field.

2.3 Electronic and Optical Properties of Graphene and Bilayer Graphene Quantum Dots (QDs)

2.3.1 Graphene in Reduced Dimensions

Right after the experimental discovery of graphene, electrical transport experiments have been done on “bulk” graphene, typically micrometer-sized Hall bars. Interesting properties like the theoretically predicted temperature-independent mobility have been demonstrated (Novoselov et al. 2004). One of the famous results is the observation of the anomalous “half-integer” quantum Hall effect (Novoselov et al. 2005; Zhang et al. 2005). It is the quasi-relativistic analog of the integer quantum Hall effect in semiconductors with a parabolic dispersion relation. Furthermore, it has been observed that the minimum conductivity in graphene does not reach zero in the limit of zero carrier density but approaches a minimum of the order of e^2/h (Tworzydło et al. 2006; Tan et al. 2007). This is an intrinsic property of 2D Dirac fermions present in graphene crystals without impurities or lattice defects (Katsnelson et al. 2006): The experimental value depends on sample geometry, disorder, and overall doping of the graphene flake (Geim and Novoselov 2007; Tan et al. 2007). The presence of the residual conductivity has strong impact on the electrostatic tunability of graphene devices (Novoselov et al. 2004), making it difficult to fully pinch off currents in 2D graphene devices.

In GNRs (which typically have a width around 100 nm), an effective energy gap can be observed (see Figure 2.3b). Ideal GNRs (Brey and Fertig 2006; White et al. 2007) promise interesting quasi-1D physics in analogy to CNTs (Saito et al. 1999; Reich et al. 2004), which can be imagined as rolled-up GNRs. The overall semiconducting behavior of GNRs allows overcoming the limitations of the gapless graphene band structure. This makes them promising candidates for the fabrication of nanoscale graphene transistors (Wang et al. 2008), tunnel barriers, and QDs (Ponomarenko et al. 2008; Stampfer et al. 2008). Electronic transport through GNRs has been studied intensively (Chen et al. 2007; Han et al. 2007; Liu et al. 2009; Stampfer et al. 2009; Todd et al. 2009) and will be discussed in more detail in Section 2.5.1.

QDs (Sohn et al. 1997) are tiny objects, typically consisting of 10^3 – 10^9 atoms. The confinement of the electrons in all three spatial directions results in a quasi-0D system within a quantized energy spectrum

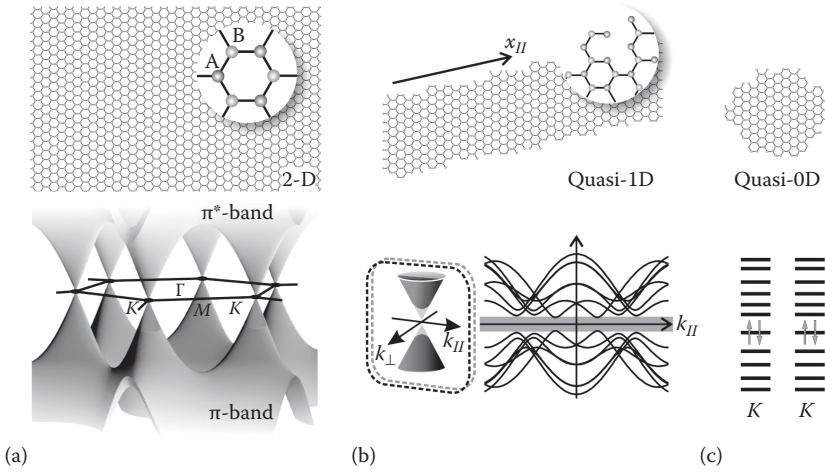


FIGURE 2.3 Graphene structures from 2D to 0D. (a) Illustration of the honeycomb-like lattice in extended graphene (2D) and the dispersion relation of graphene. (b) GNR (1D) with rough edges and schematics of the corresponding quasi-1D band structure. (c) QD (0D) in form of a nanometer-sized graphene flake and the expected discrete energy level spectrum (spin and valley degeneracy is assumed).

(see Figure 2.3c). QDs are therefore regarded as artificial atoms (Kastner 1993) where the single particle level spectrum can be set by the dimensions of the QD. The relevant energy scales in graphene QDs are discussed in Section 2.3.2. The designable level spectrum makes graphene QDs interesting for optical experiments (see Section 2.3.3). Furthermore, QDs and DQDs are regarded as promising hosts for spin qubits (Loss and DiVincenzo 1998). Because of the low spin-orbit and hyperfine interaction, graphene is of special interest. Over the past years, graphene QDs and DQDs have been studied intensively, which will be summarized in Section 2.3 and the following.

2.3.2 Relevant Energy Scales

There are several energy scales that have to be considered performing transport experiments in graphene QDs.

Coulomb energy: The Coulomb energy $E_C = E^2/C_2$ of a QD can be estimated by its self-capacitance. For QDs in planar 2DEGs, and in graphene, the QD is commonly approximated by a circular disc of radius r embedded in a material with dielectric constant ϵ (Sohn et al. 1997; Ihn 2010). Gates and contacts are neglected within this model. The self-capacitance then measures $C = 8\epsilon\epsilon_0 r$. Considering a graphene QD placed on a SiO_2 substrate, $\epsilon \approx (\epsilon_{\text{SiO}_2} + 1)/2 \approx 2.5$ can be estimated as the average dielectric constant of the substrate material and air. Experimentally observed addition energies, E_{add} , i.e., the sum of charging energy E_C and level spacing Δ in graphene QDs, are shown in Figure 2.4a.

Level spacing in single-layer graphene: The level spacing of electronic excited states (ESs) in graphene QDs can be derived from the density of states (Schnez et al. 2009; Schnez 2010). The density of states (DOS) in single-layer graphene is given by $D(E) = 2E/(\pi\hbar^2 v_F^2)$ (Castro Neto et al. 2009; Das Sarma et al. 2011). Approximating a QD by a circular island with an area $A = \pi r^2$ and number of charge carriers N , the total quantum mechanical energy is given by

$$E_{\text{QM}}(N) = A \int_0^{E_F} dE E D(E) = \frac{2A}{3\pi(\hbar v_F)^2} E_F^3. \quad (2.5)$$

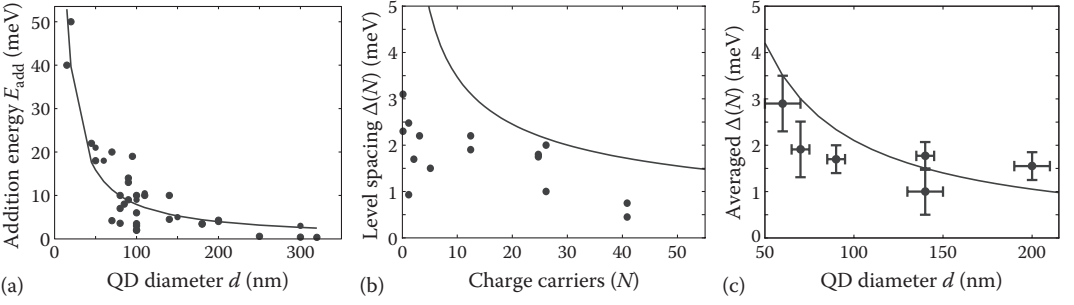


FIGURE 2.4 Addition energies and ES level spacings in graphene QDs. (a) Addition energies of single-layer and bilayer graphene QDs obtained by finite-bias spectroscopy measurements. The solid line is a fit $E_{\text{add}} \propto d^{-1}$. (b) Level spacing of the first ES as a function of the number of charge carriers on the QD estimated from finite-bias spectroscopy. The dashed line shows the theoretical energy dependence according to Equation 2.8. (c) Averaged level spacings observed in different samples as a function of effective dot diameter. The solid line shows the diameter dependence expected from Equation 2.8. (Experimental data are extracted from Ponomarenko, L.A. et al., *Science*, 320, 356, 2008; Stampfer, C. et al., *Nano Lett.*, 8, 2378, 2008; Güttinger, J. et al., *Phys. Rev. Lett.*, 103, 046810, 2009; Moriyama, S. et al., *Nano* 8, 2891, 2009; Volk, C. et al., *Nano Lett.*, 11, 3581, 2011; Volk, C. et al., *Nat. Commun.*, 4, 1753, 2013; Connolly, M.R. et al., *Nat. Nanotechnol.*, 8, 417–420, 2013; Liu, X. et al., *Phys. Rev. B*, 80, 121407, 2009; Liu, X.L. et al., *Nano Lett.*, 10, 1623–1627, 2010; Neubeck, S. et al., *Small*, 6, 14, 2010; Puddy, R.K. et al., *Appl. Phys. Lett.*, 103, 183117, 2013; Goossens, A.M. et al., *Nano Lett.*, 12, 4656–4660, 2012b; Allen, M.T. et al., *Nat. Commun.*, 3, 934, 2012; Schnez, S. et al., *Appl. Phys. Lett.*, 94, 012107, 2009; Güttinger, J. et al., *N. J. Phys.*, 10, 12029, 2008; Stampfer, C. et al., *Appl. Phys. Lett.*, 920, 012102, 2008; Molitor, F. et al., *Appl. Phys. Lett.*, 940, 222107, 2009; Güttinger, J. et al., *Phys. Rev. Lett.*, 1050, 116801, 2010; Güttinger, J. et al., *Phys. Rev. B*, 83, 165445, 2011; Güttinger, J. et al., *Nano. Res. Lett.*, 6, 253, 2011; Müller, T. et al., *Appl. Phys. Lett.*, 101, 012104, 2012; Dröscher, S. et al., *Appl. Phys. Lett.*, 101, 043107, 2012; Jacobsen, A. et al., *N. J. Phys.*, 14, 023052, 2012; Bischoff, B. et al., *N. J. Phys.*, 15, 083029, 2013; Wang, L.-J. et al., *Appl. Phys. Lett.*, 99, 112117, 2011; Wang, L. et al., *Science*, 342, 614, 2013; Zhou, C. et al., *Chin. Phys. Lett.*, 29, 117303, 2012; Wang, L.-J. et al., *Chin. Phys. Lett.*, 28, 067301, 2011; Kölbl, D., Zumbühl, D., 2013; Fringes et al., *Phys. Status Solidi B*, 248, 2684, 2011; Epping, A. et al., *Phys. Status Solidi B*, 25, 2682, 2013. Panels b and c adapted from Güttinger, J. et al., *Rep. Prog. Phys.*, 75, 126502, 2012. Copyright 2012 IOP Publishing.)

Applying the dispersion relation for single layer graphene $E = \hbar v_F |k_F|$ with $k_F = \sqrt{\pi n} = \sqrt{\pi N/A}$, Equation 3.1 can be rewritten as

$$E_{\text{QM}}(N) = \frac{2A\hbar^3 v_F^3}{3\pi(\hbar v_F)^2} k_F^3 = \frac{2\hbar v_F}{3} \sqrt{\pi/A} N^{3/2} = \frac{4\hbar v_F}{3} \frac{1}{d} N^{3/2}. \quad (2.6)$$

The chemical potential μ can be expressed as the following, where the approximation is valid in the regime of large N .

$$\mu(N) = E_{\text{QM}}(N+1) - E_{\text{QM}}(N) = \frac{4\hbar v_F}{3} \frac{1}{d} ((N+1)^{3/2} - N^{3/2}) \approx 2\hbar v_F \frac{\sqrt{N}}{d}. \quad (2.7)$$

The ES level spacing Δ is thus given by the difference

$$\Delta(N) = \mu(N+1) - \mu(N) \approx \hbar v_F \frac{1}{d\sqrt{N}}. \quad (2.8)$$

The ES level spacing in graphene QDs obtained from finite-bias spectroscopy measurements is shown as a function of the number of charge carriers in Figure 2.4b and as a function of the QD diameter in Figure 2.4c.

Level spacing in bilayer graphene: For bilayer graphene QDs, the level spacing can be calculated following the same approach taking into account the difference in density of states and dispersion relation. In the vicinity of the Dirac points, the dispersion relation of bilayer graphene is parabolic, and thus, the density of states equals the one of a 2DEG, $D(E) = \gamma_1 / (\pi \hbar^2 v_F^2)$. This is in contrast to single-layer graphene and does not depend on the energy. Thus, the total energy is quadratic in E_F :

$$E_{\text{QM}}(N) = A \int_0^{E_F} dE E D(E) = \frac{A \gamma_1}{2\pi(\hbar v_F)^2} E_F^2. \quad (2.9)$$

As derived in Section 2.2, the low-energy dispersion relation takes the form of a 2DEG, $E = \frac{\hbar^2 k_F^2}{2m^*}$ with the effective mass defined by the interlayer hopping energy: $m^* = \gamma_1 / 2v_F^2$. Thus, the energy reads as

$$E_{\text{QM}}(N) = \frac{A \gamma_1}{2\pi(\hbar v_F)^2} \left(\frac{\pi \hbar^2}{2m^*} \right)^2 \left(\frac{N}{A} \right)^2 = \frac{\pi \hbar^2 v_F^2}{2\gamma_1} \frac{N^2}{A} \quad (2.10)$$

and the chemical potential is given by

$$\mu(N) = \frac{\pi \hbar^2 v_F^2}{2\gamma_1} \frac{2N+1}{A}. \quad (2.11)$$

This results in an ES level spacing Δ , which is independent of the number of electrons on the QD (Volk et al. 2011):

$$\Delta(N) = \frac{\pi \hbar^2 v_F^2}{\gamma_1} \frac{1}{A}. \quad (2.12)$$

Tunnel coupling: The tunnel resistance R_t to the leads has to be sufficiently high such that an electron is either located in one of the leads or on the QD. The minimum R_t to fulfill this condition can be estimated according to Heisenberg's uncertainty relation $\Delta E \cdot \Delta t > h$, with the desired energy resolution ΔE and the time scale of a tunneling process $\Delta t = R_t C_\Sigma$. This yields the relation $R_t > h / C_\Sigma \Delta E$. Regarding the charging energy as the desired resolution, the condition $R_t > h/e^2$ has to be satisfied (Sohn et al. 1997; Ihn 2010).

Thermal energy: The thermal broadening of a Coulomb peak is proportional to $\cosh^{-2} \left(\frac{\alpha e \Delta V_G}{2k_B T} \right)$. This implies that the temperature has to be sufficiently low to resolve Coulomb charging effects ($k_B T \ll E_C$) and the ES spectrum ($k_B T \ll \Delta$).

2.3.3 Optical Properties

Because of the absence of a bandgap, no optical luminescence is observed in extended graphene sheets. It has been shown that a bandgap can be induced by shaping graphene into nanoribbons (GNRs) and dots (QDs) due to quantum confinement (Ponomarenko et al. 2008; Li and Yan 2010) and edge effects (Zhu et al. 2011), which will be discussed in Section 2.5.1. Theory predicts a $1/d$ dependence of the induced confinement gap on the QD diameter d . Graphene QDs have been studied with optical methods like absorption spectroscopy, PL, and PLE.

Figure 2.5a shows the ultra violet (UV)-visible absorption spectra of chemically synthesized graphene QDs of different diameters (Peng et al. 2012). A blue shift from 330 to 270 nm with decreasing size is

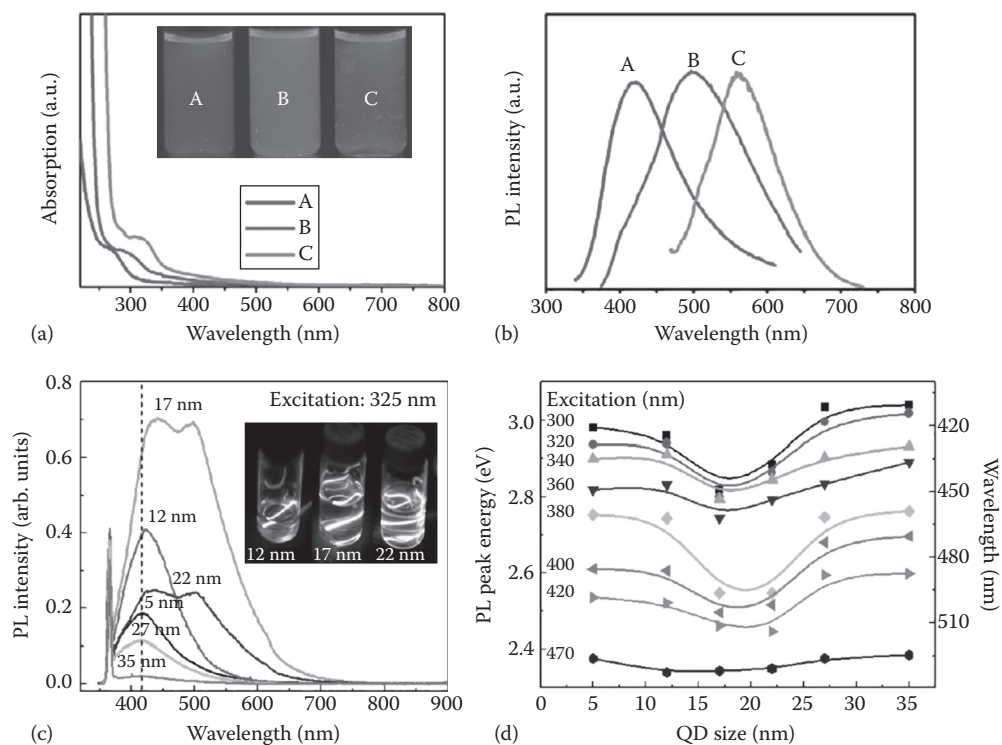


FIGURE 2.5 Optical properties of graphene QDs. (a) Absorption spectra in the UV to visible regime of solutions containing graphene QDs synthesized from carbon fibers under different conditions. The average diameter of the QDs measures 2–4 nm, 5–7 nm, and 8–10 nm respectively in samples A, B, and C. Inset: Photograph of the corresponding graphene QDs under UV light with 365 nm. (b) PL spectra of the QDs in panel a showing different emission colors. (c) PL spectra excited at 325 nm for graphene QDs of 5–35 nm average sizes in deionized (DI) water. Inset: different colors of luminescence from QDs depending on their average size (12, 17, and 22 nm). (d) PL peak energy as a function of the QD diameter measured with different excitation wavelengths from 300 to 470 nm. (a and b, Reprinted with permission from Peng, J. et al., *Nano Lett.*, 12, 844, 2012. Copyright 2012 American Chemical Society. c and d, Reprinted with permission from Kim, S. et al., *ACS Nano*, 6, 8203, 2012. Copyright 2012 American Chemical Society.)

observed. The inset shows the optical images of solutions containing three sizes of graphene QDs under UV light. Figure 2.5b shows the PL spectra of the same QDs.

Figure 2.5c shows PL spectra of graphene QDs synthesized by chemical cutting of graphene sheets obtained by thermal deoxidization of graphene oxide sheets (Kim et al. 2012). A clear size-dependent emission energy can be observed. Interestingly, the energy first decreases with increasing diameter, which is in agreement with the quantum confinement effect in graphene. Above $d = 17$ nm, the energy increases again (see Figure 2.5d).

These experiments show that the emission and absorption spectra of graphene QDs are size dependent, which is in agreement with the theory assuming a size-dependent confinement gap.

2.4 Fabrication of Graphene Nanostructures

2.4.1 Top-Down Approach

The most common technique to fabricate graphene nanostructures for electronic transport experiments is based on micromechanical exfoliation of graphene from natural bulk graphite followed by

lithography and dry etching. This fabrication process dates back to the early ages of graphene and has been introduced by Novoselov et al. (2004, 2005) and Zhang et al. (2005). Alternative techniques as local anodic oxidation (Neubeck et al. 2010) or soft confinement of electrons in bilayer graphene (Allen et al. 2012; Goossens et al. 2012b) have been demonstrated more recently.

Although a lot of progress has been made in the growth of graphene over the past years, graphene flakes exfoliated from natural bulk graphite still provide the best crystal quality. Thus, research, especially transport experiments, is mainly carried out on such flakes. The technique of micromechanical exfoliation, often referred to as “Scotch tape technique,” makes use of the fact that in graphite, the individual graphene layers are only weakly bond by van der Waals forces, in contrast to the strong covalent intralayer bonds. This allows overcoming the interlayer bonds using an adhesive tape and thus cleaving of individual graphene sheets from a graphite crystal. The graphene flakes are deposited on prepared silicon chips with a SiO₂ top layer (see Figure 2.7a and b). Graphene is highly transparent (absorption \approx 2.3%), but thanks to interference effects, the visibility of graphene can be increased by tuning the oxide thickness and the wavelength of the incident light. It has been shown that the contrast has maxima at oxide thicknesses of 90 and 300 nm for green light ($\lambda \approx$ 550 nm) (Novoselov et al. 2004; Blake et al. 2007; Tombros 2008). Raman spectroscopy is used to reliably identify single-layer and bilayer graphene (Ferrari et al. 2006; Gupta et al. 2006; Graf et al. 2007; Malard et al. 2009) among the flakes that have been deposited onto the substrate. Figure 2.6 shows the differences between the Raman spectra measured on a single-layer and a bilayer graphene flake. A detailed study of Raman spectra of graphitic flakes of different thicknesses can be found in Graf et al. (2007).

Plasma-based reactive ion etching (RIE) is commonly used to pattern graphene nanostructures (Novoselov et al. 2005; Zhang et al. 2005; Güttinger et al. 2012). The sample is coated with a resist, typically polymethylmethacrylate (PMMA). An etch mask is designed individually for each graphene flake, which is transferred to the resist by electron beam lithography (EBL) (see Figure 2.7c). With thin resist layers (\approx 50 nm) and optimized EBL parameters, structures as narrow as 20 nm can be routinely defined. After development, the graphene is etched by RIE. The advantage of dry etching is its high anisotropy and selectivity. It has been proven that this technique does not introduce bulk defects in the graphene sheet (Bischoff et al. 2011). For example, an argon/oxygen plasma (20% O₂) combines the physical impact of the argon with the chemical reactivity of the oxygen ions. Short etching times of typically below 10 s and low power (60 W) are sufficient to etch graphene. With increasing etching time or increasing power, the PMMA is cross-linked, making it challenging to remove it with organic solvents. Common treatments to remove hardened resist like oxidizing acids or plasma ashing cannot

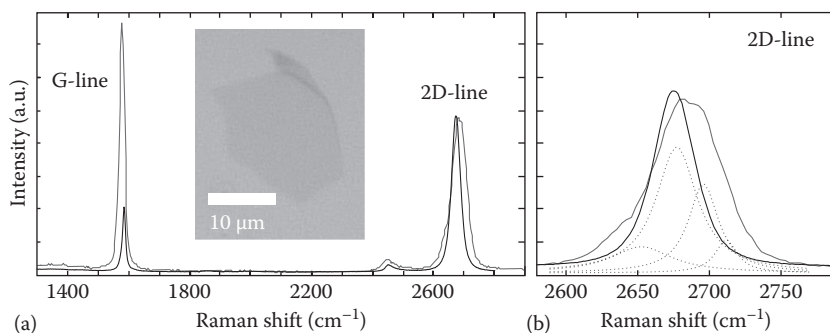


FIGURE 2.6 Raman spectroscopy on single-layer and bilayer graphene. (a) Comparison of the Raman spectra of single-layer graphene (black curve) and bilayer graphene (gray curve). In single-layer graphene, the 2D-line is often twice as high as the G-line. The inset shows an optical micrograph of a single-layer graphene flake on a Si/SiO₂ substrate. (b) Close-up on the 2D-lines shown in panel a. The bilayer 2D-Raman peak can be described by four Lorentzian line shapes (see dotted lines). (Data from Volk, C. et al., *Nano Lett.*, 11, 3581, 2011; Volk, C., Neumann, C., Kazarski, S. et al., *Nat. Commun.*, 4, 1753, 2013.)

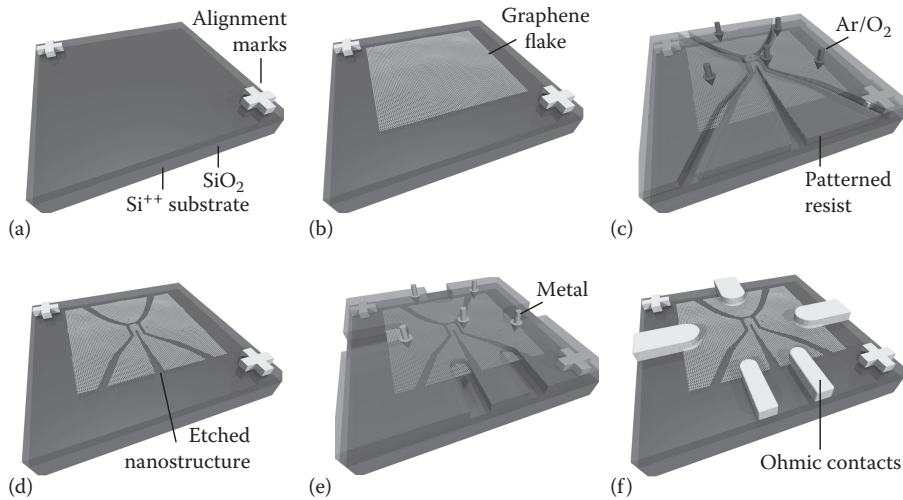


FIGURE 2.7 Typical process flow to fabricate graphene QD devices. (a) Highly p-doped Si substrate covered by 295 nm SiO₂ (see labels). Metal alignment marks have been deposited for further lithography steps. (b) Exfoliated graphene flake. (c) A layer of polymer resist has been patterned by EBL. The graphene is etched by an Ar/O₂-plasma (indicated by arrows). (d) Etched graphene nanostructure after removal of the resist. The example shows a graphene QD with three lateral gates. (e) Deposition of ohmic contacts by metal evaporation (typically Cr/Au) after a second EBL step. (f) Device after contacting which is now ready for measurements.

be used as these will remove graphene as well. The schematic in Figure 2.7d shows the etched graphene nanostructure.

Metal contacts connecting the graphene devices to bond pads are defined by an additional EBL, metallization, and lift-off step (see Figure 2.7e). A thin layer (typically 2 to 5 nm) of Cr or Ti is deposited as an adhesion layer, followed by 50 nm Au or Pt, leading to typical contact resistances in the range of kΩ. Figure 2.7f shows a contacted graphene QD device. Transmission line measurements have shown that graphene/metal contact resistances can be potentially reduced by using palladium (Song et al. 2012; Watanabe et al. 2012). However, in graphene nanostructures, the contact resistance is not very crucial since the resistance is limited by the nanostructure itself.

2.4.2 Bottom-Up Approach

Besides the fabrication technique based on EBL, graphene QDs have been fabricated, e.g., by ruthenium-catalyzed C60 transformation (Lu et al. 2011) suffering from extremely expensive raw materials and low yield. Graphene QDs prepared by multistep hydrothermal (Pan et al. 2010) or electrochemical strategies (Li et al. 2010) from graphene oxide have shown blue or green luminescence. As the bandgap in graphene QDs is size dependent, a controlled size of the QDs is especially important for PL emission. It has been shown that graphene QDs can be synthesized by wet chemical oxidization and cutting of micrometer-sized carbon fibers (see Figure 2.8a) (Peng et al. 2012). Commercially available carbon fibers are added into a mixture of concentrated H₂SO₄ and HNO₃. The solution is first sonicated and then stirred at different temperatures between 80°C and 120°C. The mixture is cooled and the pH is adjusted to 8 with Na₂CO₃. The final product solution is further dialyzed for 3 days (Peng et al. 2012). The as-synthesized graphene QDs are highly soluble in water and other polar organic solvents. Their lateral size ranges from 1 to 4 nm, and the QDs are typically one to three atomic layers thick. Figure 2.8b shows a high-resolution transmission electron microscopy (HRTEM) image of a graphene QD. The arrows indicate the zigzag direction of the lattice. The corresponding fast Fourier transform (FFT) pattern is shown in the inset.

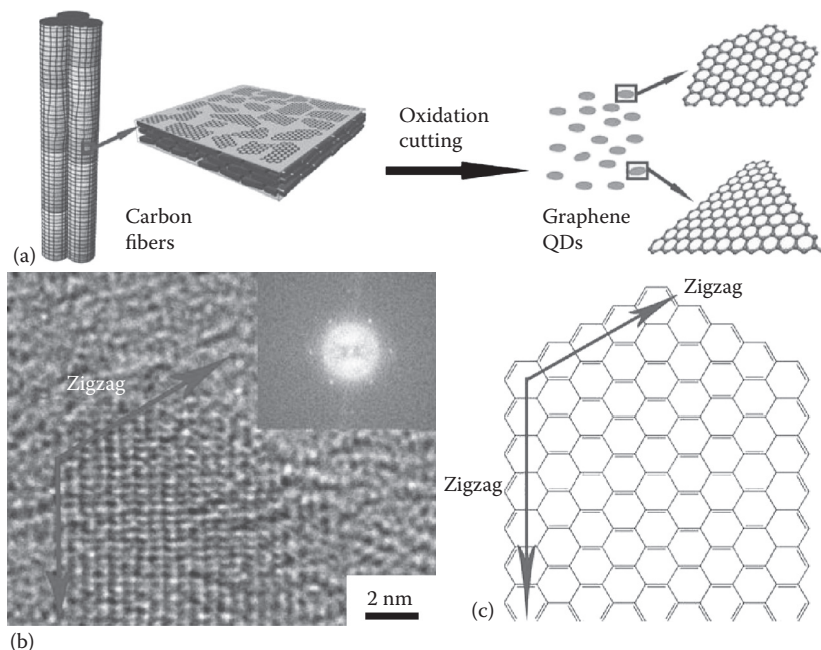


FIGURE 2.8 Chemical synthesis of graphene QDs. (a) Illustration of the wet chemical oxidation cutting of carbon fibers into graphene QDs. (b) High-resolution transmission electron micrograph of a graphene QD. The arrows indicate the zigzag edges of the QD. Inset: 2D FFT of the edge. (c) Schematic representation of the edge termination of the HRTEM image in panel b. (Reprinted with permission from Peng, J. et al., *Nano Lett.*, 12, 844, 2012. Copyright 2012 American Chemical Society.)

2.5 Graphene Single-Electron Transistors and QDs

2.5.1 GNRs and Nanostructures

As GNRs are building blocks of most graphene quantum devices, this section summarizes the relevant transport properties of these structures.

From CNTs, which can be imagined as rolled-up GNRs, it is well known that a bandgap opens depending on their orientation and their diameter (Saito et al. 1999). The orientation of CNTs is named after their circumference, while GNRs are classified according to their edges along the ribbon. N -aGNRs and N -zGNRs commonly denote armchair (a) and zigzag (z) GNRs with N dimers across the ribbon width. The zGNRs and aGNRs are well understood in theory. The band structure can be determined by applying vanishing boundary conditions to the Dirac Hamiltonian of graphene. In zGNRs, one edge is made up by A atoms, and the other one, by B atoms, and thus, the boundary condition can be applied to the sublattices separately. In aGNRs, the edges contain atoms of both sublattices, and thus, the boundary condition has to be fulfilled by both sublattices (Brey and Fertig 2006).

Alternatively, the band structure can be determined following a tight-binding approach depending on the orientation and the width of GNRs. Armchair GNRs have a metallic band structure if the condition $N = 3m - 1$ with integer m is fulfilled. Otherwise, a semiconducting band structure occurs (Kastner 1993; Nakada et al. 1996; Cresti et al. 2008). The bandgap E_g scales inversely with the ribbon width W . An estimate is given by Saito et al. (1999) and Güttinger (2011)

$$E_g = 2\hbar v_F \Delta k_F = 2\pi\hbar v_F / W, \quad (2.13)$$

where Δk_F is the minimum allowed wave number across the ribbon width.

Density functional theory (DFT) calculations taking into account next-nearest-neighbor hopping and a contraction of the bond length at the edges have shown that even metallic aGNRs have at least a small bandgap that depends on the ribbon width (Son et al. 2006). Zigzag GNRs have a gapless band structure independent on N . First-principle calculations have shown a high density of zero-energy states at the edges, which has been proved by scanning tunneling spectroscopy (Kobayashi et al. 2005). Magnetic ordering at the edges may lead to the opening of a small bandgap in zGNRs (Wakabayashi et al. 1999; Son et al. 2006).

Theory assumes either pure armchair or pure zigzag GNRs, where the edges are terminated by hydrogen atoms. Using common experimental techniques, it has not yet been possible to fulfill these conditions. Typically, arbitrary edges occur when GNRs are etched out of graphene sheets. When using an O_2 -based plasma as the etchant, the edges will probably be oxygen terminated. In the following, electronic transport through GNRs will be described on a more phenomenological basis.

Field effect measurements have proven the presence of a transport gap (see, e.g., Figure 2.9a and b and Stampfer et al. [2009]; Terrés et al. [2011]), but still a number of sharp resonances can be observed within this gap. A common model to describe the electronic transport through etched GNRs (i.e., nanoribbons with rough edges) is based on stochastic Coulomb blockade (Sols et al. 2007; Stampfer et al. 2007). A disorder potential (e.g., substrate or edge disorder) can form electron and hole puddles close to the charge neutrality point. Because of the absence of a bandgap in bulk graphene and of the presence of the effect of Klein tunneling (Katsnelson et al. 2006), transport between the electron and hole regions is possible. The situation is different in nanoribbons, where a width-dependent confinement gap separates electrons and hole puddles. Thus, effectively, a large number of QDs or localized states formed and only tunneling transport is possible (Stampfer et al. 2009; Todd et al. 2009).

The presence of QDs has been demonstrated by finite bias spectroscopy measurements on GNRs (Molitor et al. 2009; Stampfer et al. 2009; Todd et al. 2009; Terrés et al. 2011). Most importantly, two characteristic energy scales can be extracted, the effective energy gap E_g and the transport gap ΔV_g (see Figure 2.9b).

The transport gap (Figure 2.9c) is correlated with the maximum amplitude of the disorder potential. An effective energy gap E_g can be defined by the largest observed charging energy corresponding to the smallest QD. It has been shown that this energy gap only weakly depends on the length of the nanoribbon (Terrés et al. 2011). The width dependence can be modeled by

$$E_g(W) = \alpha/W e^{-\beta W}, \quad (2.14)$$

(see Figure 2.9d and Han et al. [2007]; Molitor et al. [2010b]; Stampfer et al. [2011]).

2.5.2 Single-Electron Transistors

A SET can be imagined as a conductive island that is weakly coupled to lead electrodes, and its electrochemical potential can be controlled by at least one gate electrode. A simple model of such a configuration is illustrated in Figure 2.10a. Tunneling transport between the QD and the leads is allowed; the gate is coupled only electrostatically. Electronic transport through a SET is dominated by the Coulomb blockade effect, which is a consequence of the Coulomb interaction of electrons on the island leading to a repulsive force. Thus, a certain amount of energy—the so-called charging energy E_C —has to be supplied to add an additional electron to the island. Assuming the temperature and the bias voltage are small compared with the charging energy, electron transport is possible only if the electrochemical potential of the island is positioned between the electrochemical potentials of the source and the drain lead (the so-called transport window). An electron from the source lead can now enter the island and subsequently leave to the drain lead. The system is in the regime of sequential tunneling and a current can flow. If no level is in the transport window, the number of electrons occupying the island is fixed. The system is in Coulomb blockade (see Figure 2.10b). The potential of the island can be controlled by

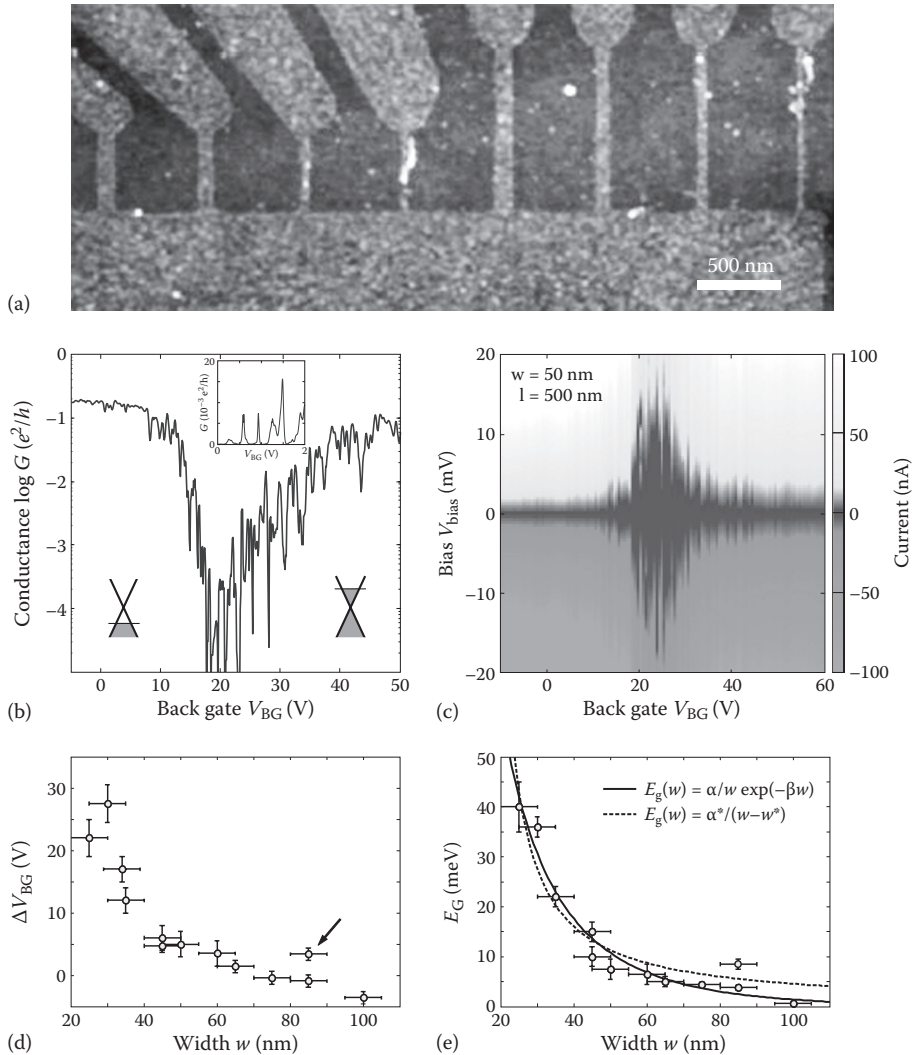


FIGURE 2.9 Characteristics of etched GNRs. (a) Scanning force micrographs of etched GNRs with different lengths and widths. (b) Conductance through a GNR (50 nm wide, 500 nm long) as a function of the back gate voltage and, thus, the Fermi level. Regions of electron and hole transport are separated by a transport gap. The inset shows a measurement within the transport gap of a 200-nm-wide nanoribbon. (c) Finite bias spectroscopy measurement allowing determination of the effective energy gap E_g and the transport gap correlated with ΔV_{BG} . (d) Transport gap as a function of the width of different nanoribbons. (e) Effective energy gap as a function of the width. Two models are fitted to the experimental data. (a–c, Reprinted with permission from Terrés, B. et al., *Appl. Phys. Lett.*, 98, 032109, 2011. Copyright 2011, American Institute of Physics. d and e, Adapted from Molitor, F., Stampfer, C., Güttinger, J. et al., *Semicond. Sci. Technol.*, 250, 034002, 2010. Copyright 2010 IOP Publishing.)

gates. Thus, measuring the current as a function of the gate voltage, regimes of conductance and of Coulomb blockade alternate, so-called Coulomb peaks, appear (see Figure 2.10d). The proportionality between the peak spacing ΔV_G and the addition energy is given by the lever arm $\alpha = E_{\text{add}}/e\Delta V_G = C_G/C_\Sigma$. It is a measure for the capacitive coupling of a gate to the QD.

By bias spectroscopy measurements, the current through a SET is recorded both as a function of the bias and the gate voltage. Diamond-shaped regions (so-called Coulomb diamonds) of suppressed

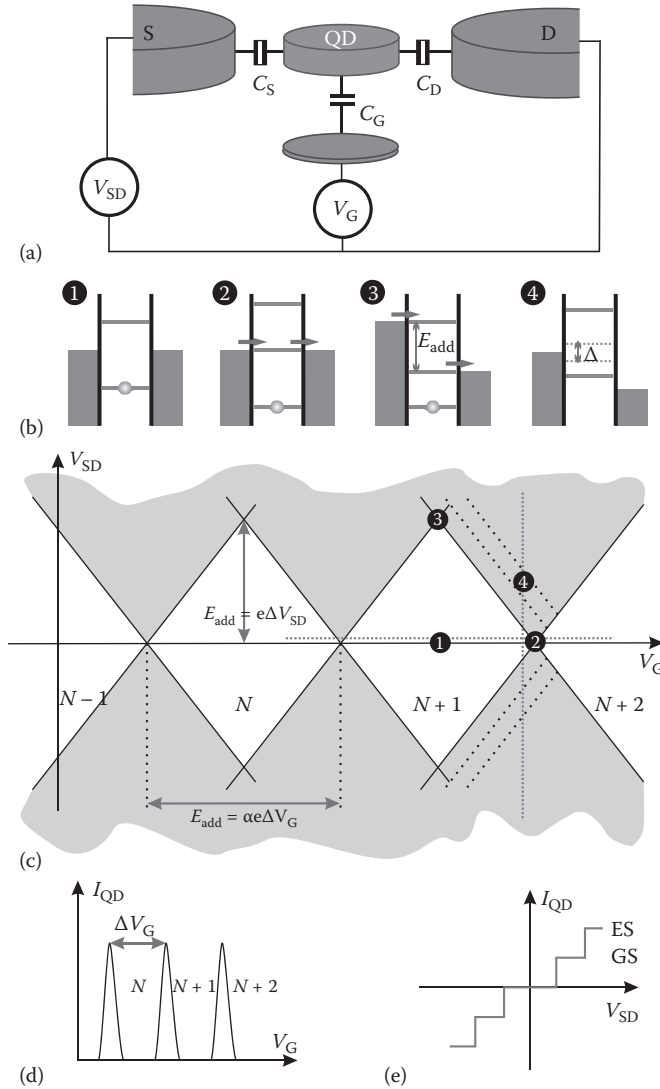


FIGURE 2.10 Transport through QDs. (a) Simple model of a QD capacitively coupled to the source and drain leads (C_S, C_D) and to one gate (C_G). Tunneling transport between the QD and the leads is allowed. These tunnel junction can be modeled by a capacitance and a resistance in parallel. (b) Schematics of four different configurations of a QD: (1) Zero bias and misalignment of the QD states with the lead potentials. (2) A QD state aligned with lead potentials. (3) The bias equals the addition energy. At least one state is within the transport window. (4) GS and first ES are aligned within the transport window; two possible transport channels are open. (c) Illustration of finite bias spectroscopy measurements on a QD. The current I_{QD} is plotted as a function of the bias V_{SD} and the gate voltage V_G . In the white regions, the device is in Coulomb blockade. The current and the number of electrons on the QD are fixed. In the gray shaded regime, transport occurs. The lever arm α is the proportionality factor between the addition energy E_{add} and the change in gate voltage ΔV_G necessary to add the next electron to the QD. (d) Cut along the gate axis at a small bias (horizontal line in panel c). Coulomb peaks with a spacing of ΔV_G appear. (e) Cut along the vertical line in panel c. The current increases each time another ES enters the transport window.

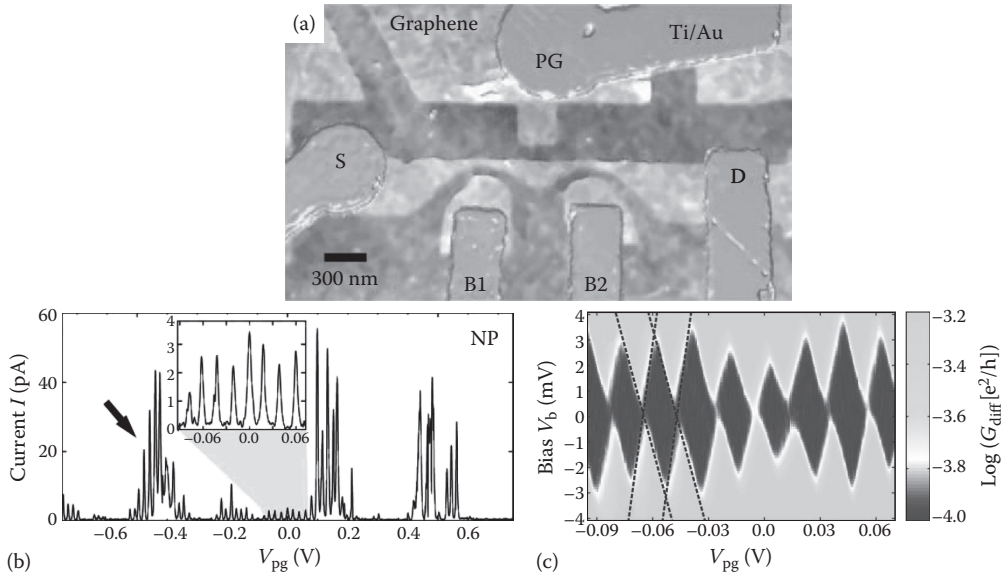


FIGURE 2.11 SET in a width-modulated graphene nanostructure. (a) False color scanning force micrograph of the device. Three lateral graphene gates are designed to locally tune the potential of the nanostructure. (b) Current through the SET as a function of the gate voltage. The inset shows a series of Coulomb peaks proving the operation as a SET. (c) Finite bias spectroscopy measurement in the same regime. (Reprinted with permission from Stampfer, C. et al., *Nano Lett.*, 8, 2378, 2008. Copyright 2008, American Chemical Society.)

conductance occur when the system is in Coulomb blockade (see schematics in Figure 2.10c). Within such a region, the number of charge carriers on the QD is constant. The extent of the diamonds in bias direction is a measure of the addition energy. Employing the gate lever arm α , the gate voltage axis can be converted into an energy scale ($E = \alpha eV_G$).

SETs have been fabricated by carving the desired shape out of graphene sheets using EBL followed by RIE (see Section 2.4). These devices consist of a graphene island connected to the source and drain electrodes via two GNRs. The devices make use of the fact that because of the narrow width of the GNRs, an effective transport gap is opened (see Section 2.5.1), and thus, they can be operated as tunable tunneling barriers. According to Equation 2.14, the gap scales approximately inversely with the ribbon width. Width modulation allows tailoring the transport gap along the ribbon axis. Close-by graphene gates and a global back gate tune the Fermi level in the nanostructure. A scanning force micrograph of a representative device is shown in Figure 2.11a. Carefully tuning the voltages on the two outer gates (B1 and B2), it is possible to bring the device into a regime where the transport gaps of both constrictions cross the Fermi level. The central island is electrically isolated, and only tunneling transport is possible between the island and the leads. The device can be operated as a SET. A series of distinct Coulomb peaks recorded as a function of the plunger gate voltage is shown in Figure 2.11b. A charging energy of ≈ 3.4 meV has been determined by finite bias spectroscopy measurements (see Figure 2.11c) on a graphene SET with 50 nm wide tunneling barriers and a central island measuring approximately 180×750 nm (Stampfer et al. 2008b).

2.5.3 QDs in Width-Modulated Nanostructures

The concept of width-modulated GNRs described in the previous section can be employed to design a graphene QD device. The smaller the central graphene island the more relevant quantum confinement effects become. Figure 2.12a shows a typical example of a graphene QD with lateral graphene gates.